Hydro-mechanical simulation and analysis of induced seismicity for a hydraulic stimulation test at the Reykjanes geothermal field, Iceland

Eirik Keilegavlen [a], Laure Duboeuf [b], Anna Maria Dichiarante [b], Sæunn Halldórsdóttir [a], Ivar Stefansson [a], Marcel Naumann [c], Egill Árni Guðnason [d], Kristján Ágústsson [d], Guðjón Helgi Eggertsson [e], Volker Oye [b], Inga Berre [a,*]

[a] Center for Modeling of Coupled Subsurface Dynamics, University of Bergen, P.O.Box 7803, 5020 Bergen, Norway
[b] Department of Applied Seismology, NORSAR, Gunnar Randers Vei 15, 2007 Kjeller, Norway
[c] Equinor ASA, Sandsliveien 90, 5254 Sandsli, Norway
[d] ÍSOR Iceland Geosurvey, Grensásvegi 9, 108 Reykjavík, Iceland
[e] HS Orka, Svartsengi, 240 Grindavík, Iceland

ARTICLE INFO

ABSTRACT

The combination of seismic analysis with advanced physics-based simulation provides an opportunity to further understand injection-induced fault reactivation, including the hydro-mechanical interplay between different faults and the rock where they reside. Here, this is investigated based on data from hydraulic stimulation of a well at the Reykjanes geothermal field. Central is the development of an interdisciplinary framework for integration of different data types towards a 3D, hydro-mechanical and faulted geothermal reservoir simulation model. This work shows how seismic interpretations can improve simulation models and, reciprocally, how fully coupled physics-based modeling can add to seismic interpretations in analysis of fault reactivation.

1. Introduction

Most of the Earth's accessible geothermal energy is stored in hard, competent rock. In such rock types, fractures and faults are the main conduits for fluid flow, which is essential for production of geothermal fluid to the surface. To enhance permeability in such formations, fluids at elevated pressures can be injected to cause slip and dilation of existing fractures or faults. This stimulation mechanism has proved successful for permeability enhancement for several geothermal reservoirs (Chabora et al., 2012; Genter et al., 2010; Schindler et al., 2010; Zimmermann & Reinicke, 2010). The stimulated slip and dilation might be realized as microseismic events, microearthquakes, or even larger earthquakes emitting seismic waves. These waves of small elastic deformations can be recorded by local seismic networks; hence, such fracture reactivation can be continuously detected, located, and analyzed in real time. In general, the stimulation aims to induce only small seismic events of magnitudes $M_w < 2$ (Ellsworth, 2013), but larger events have also been linked to hydraulic stimulation of fractured geothermal reservoirs. The most prominent are the 2017 M_w 5.4 Pohang earthquake in South-Korea (Ellsworth et al., 2019; Grigoli et al., 2018; Kim et al., 2018) and the

2006 ML 3.4 earthquake related to the Basel EGS project (Häring et al., 2008; Mukuhira et al., 2013; Deichmann & Giardini, 2009). In Iceland, the most prominent induced seismicity has been two magnitude 4 events that were observed related to geothermal wastewater reinjection in Húsmúli at the Hellisheidi geothermal area, with flow rates reaching 500 kg/s (Juncu et al., 2020).

Reactivation of fractures occurs in an interplay between coupled hydraulic, thermal, mechanical, and chemical reservoir processes and the fractured structure of the formation. To design hydraulic stimulation operations while mitigating induced seismicity, understanding of these coupled, nonlinear dynamics is crucial. In this, physics-based numerical models can provide valuable insights: either as a tool to forecast outcomes of a stimulation or to complement time-dependent data in understanding the governing mechanisms and structural features at depth.

Several physics-based numerical modeling studies have considered how an increase in pore pressure reduces effective stress on preexisting fractures or faults, thus causing slip. Early contributions include those by Rahman et al. (2002), Bruel, (2007), Kohl & Mégel (2007), Baisch et al. (2010), and McClure & Horne (2011). To incorporate the important effect of stress redistribution due to fracture reactivation is challenging;

* Corresponding author.
E-mail address: inga.berre@uib.no (I. Berre).

even the more advanced numerical models accounting explicitly for the structural effect of large-scale fractures and faults are typically based on strong simplifications of the physics governing flow, mechanics, or coupled hydromechanics related to the fractures and/or the domain surrounding them (McClure and Horne, 2011; Norbeck et al., 2016; Ucar et al., 2017, 2018a). Recently, however, numerical modeling tools which consider networks of fractures or faults in 3D domains have been developed that consistently account for fully coupled hydro-mechanical processes as well as fracture-contact mechanics (Berge et al., 2020; Gallyamov et al., 2018; Garipov et al., 2016; Garipov & Hui, 2019; Berre et al., 2020; Keilegavlen et al., 2021). The application of these advances within modeling to field studies has, however, been limited. To further understand hydro-mechanical fault reactivation, there is a need for improved integration between the interpreted monitoring results obtained from real field data observations and the input variables required for the numerical modelling. In this work, we will consider a specific case study for a stimulation test at the Reykjanes geothermal field in SW Iceland on 29 March 2015.

The large-scale exploitation of the Reykjanes field for geothermal energy started when Hitaveita Suðurnesja (Reykjanes District Heating), now HS Orka, acquired the development concession rights for the geothermal field and drilled its first well for electrical generation in 1998. In 2006, production started at the 100 MWe Reykjanes power plant. As of 2019, a total of 37 wells have been drilled in Reykjanes for exploration, production, and re-injection. The conceptual model of the geothermal system is described by Khodayar et al. (2018), Weisenberger et al. (2019), and Nielsson et al. (2020).

In 2014 and 2015, the wells RN-33 and RN-34 were drilled from a well pad northwest of Sýrfell, about 2 km northeast of the center of the main production area (Fig. 1c). The wells were intended for re-injection of separated brine from the Reykjanes Power Plant. Well RN-33 is directionally drilled to the SW and connected to the production field through a NE-SW trending fissure zone. Re-injection in this well started early December 2013 and was stable at around 50 L/s until early June 2014, when it was stopped until re-injection restarted in March 2016. Well RN-34 is directionally drilled to the NW and results of tracer tests indicate that the well is not hydraulically connected to the production field. For RN-34 a fall-off test followed by 10 hours of cyclic stimulation was conducted on 29 March 2015 (Supporting Material, Texts S3 and S4). Afterwards, continuous injection started on 20 May 2015. Seismic events related to the injections were observed near the injection point (Blanck et al. 2020).

In this paper, we aim to study how simulations based on state-of-the art hydro-mechanical numerical models can complement data in an investigation of fault reactivation. We present an investigation of the hydraulic stimulation of RN-34 based on new analysis of the seismic data combined with an unprecedented simulation study of the reservoir dynamics. Based on all available data relevant to the study of the hydraulic stimulation test, we develop a novel hydro-mechanical model of the faulted reservoir to simulate the subsurface dynamics that occur as a response to hydraulic stimulation. For the simulation, we employ a simulator constructed for fully coupled flow, poroelasticity, and fracture deformation (Keilegavlen et al., 2021). The advanced simulation model accounts for flow in both explicitly represented faults and the low-permeable surrounding porous medium, slip of faults based on a Coulomb friction law, and coupled poroelastic response of the porous medium to fluid pressure and fault slip. To our knowledge this represents the first application of a simulator constructed for fully coupled poroelasticity and fracture deformation to model stimulation of an actual geothermal reservoir.

The paper is structured as follows: In Section 2, we present the regional context of the RN-34 stimulation test site, including regional information for the stress state and a model of the dominating fault geometry near RN-34. Furthermore, seismicity due to the continuous injection that started 20 May 2015 is presented, providing additional information for the fault model. Section 3 presents observations related to the 29 March 2015 RN-34 stimulation, including measurements of pressure and flow rates in the injection well and analysis of induced seismicity. In Section 4, we present the mathematical model and the simulation model, including parameter identification based on well data. Section 5 presents the numerical model and simulation results. A discussion of the combined results from seismic analysis and physics-based simulations is given in Section 6, followed by a summary and concluding remarks in Section 7.

## 2. From regional geological context to local fault model geometry

To model the coupled dynamics of a geothermal reservoir and analyze microseismic data, consideration of the target area's geological setting is important. This includes how the setting dictates today's local stress field conditions. Specifically, identification of the local fault network and stress field conditions are necessary. They are determined from the regional geological data, profiles derived from active seismic data, local earthquake observations, and microseismic data. Thus, in this section, we first introduce the regional geological setting: the larger structures and stresses that surround our target area. Then, we bring these into context with existing local-scale geological interpretations and recent seismological observations, which are integrated to understand the stresses that acted at a given time on certain faults involved in the local model.

The fault and fracture orientation reading convention used in this paper is strike (0°–360°)/dip (0°–90°) and rake (hanging-wall slip vector is measured on the plane of the fault) for recording fault planes/focal planes and their relative kinematics and trend (0°–360°)/plunge (0°–90°) for stress axes. Both conventions follow the right-hand rule, and both stereonets and focal mechanisms are projected on the lower hemisphere.

2.1. Regional geological setting

Iceland is located at a complex mid-ocean ridge plate boundary between the Eurasian and American plates (Fig. 1a), coinciding with a relatively large amount of hot, upwelling mantle material, which explains its volcanic activity. The Reykjanes geothermal field is located on the southwest tip of the Reykjanes Peninsula Transtensional Zone (RPTZ) in SW Iceland, where the Reykjanes Ridge (RR) comes onshore and the plate boundary changes direction. Rifting becomes oblique on the RPTZ and the rift segments split into a series of NE-SW trending eruptive fissures, which can be grouped into four en échelon volcanic fissure swarms (Sæmundsson, 1978). The fissure swarms, from east to west, Hengill, Brennisteinsfjöll, Krýsuvík and Reykjanes-Eldvörp-Svartsengi (for location see Fig. 1 in Keiding et al., 2009), consist of normal faults and tension fractures in addition to the eruptive fissures. They are intersected by a series of near vertical N-S trending right-lateral strike slip faults (Keiding et al., 2009). The regional extension direction of this oblique rift (extension is not orthogonal to plate boundary) is N101-103°E with an extension rate of 19–20 mm/yr along both active rift and transform segments (e.g., Keiding et al., 2009).

The patterns of natural seismicity are valuable in understanding the complex geological structures of the Reykjanes Peninsula (see, e.g., Björnsson et al., 2020, and Keiding et al., 2009). Based on GPS measurements taken during the 1993 and 1998 seismic swarm events, which showed almost exclusively strike-slip deformation, Clifton and Kattenhorn (2006) interpreted the geological structural complexity in Reykjanes, concluding that, to accommodate oblique spreading, episodes of tectono-magmatic activity (during extension) and episodes of left-lateral strike-slip motion alternate with different periodicity and in different structural blocks. However, fault plane solutions computed from two of many earthquake swarms on the Reykjanes Peninsula (in 1972 and 2013) showed that both normal, strike–slip, and oblique motions occurred during both earthquake swarms in a magmatic phase
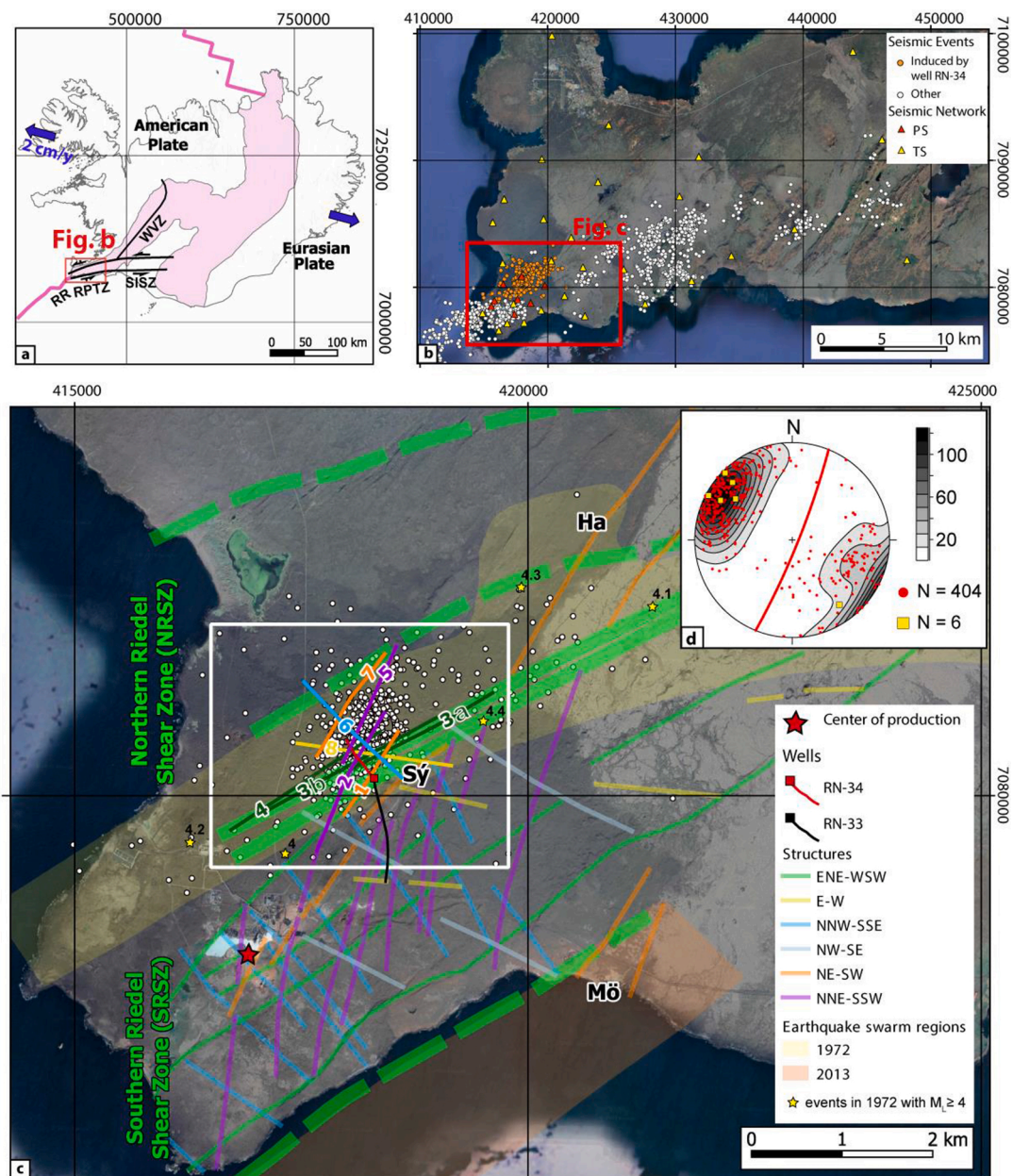
Fig. 1. (a) Plate boundary across Iceland showing the study location (red box); the Reykjanes Peninsula Transtensional Zone (RPTZ) is located in the region where the Reykjanes Ridge (RR), South Iceland Seismic Zone (SISZ), and the Western Volcanic Zone (WVZ) meet. The plate boundary (line) and rocks of age less than 0.8 Ma (adapted from Khodayar et al., 2018) are shown in pink. (b) The Reykjanes Peninsula showing the two networks (yellow and red triangles, respectively) for the temporary seismic (TS) network and the permanent seismic (PS) network as well as the re-located seismic events (shown by white and orange dots). The events analyzed in this study are those shown by the orange dots. (c) Simplified structural map of the Reykjanes geothermal field adapted from Khodayar et al. (2018) showing boundaries of the two major Riedel shear zones: the Northern Riedel Shear Zone (NRSZ) and the Southern Riedel Shear Zone (SRSZ). Also shown are the outlines of the 1972 (yellow) and 2013 (orange) earthquake swarms as well as events from the 1972 swarm (Klein et al. 1977, Björnsson et al., 2020) with $M_L \geq 4$ (yellow stars). Structures are shown as transparent lines in the SRSZ and elsewhere and the initial considered fault model is shown using non-transparent numbered lines in the studied area. For both, the color scheme is based on orientation. Induced seismic events are shown in white. The locations Sýrfell (Sý), Mölvík (Mö), and Haugur (Ha) are shown. The wellhead location of wells RN-34 and RN-33 is marked with a square and the well paths with lines. The approximate location of the center of production is indicated by a red star and the study area by a white rectangle. The relocated events analyzed in this study are those shown by white dots. (d) Equal area stereonet plot and density contour of the fractures interpreted from well RN-34 by Árnadóttir et al. (unpublished report, Supporting Material, Text S1). Fractures are represented as poles to planes (red dots), and fractures with a mechanical aperture >19 mm as yellow squares (Supporting Material, Table S2). Mean

orientation of fractures interpreted with high confidence is represented by a large red circle (Supporting Material, Table S1). (For interpretation of the references to color in this figure legend, the reader is referred to the web version of this article.)

(Björnsson et al., 2020; Khodayar et al., 2018), supporting the idea that deformation might occur simultaneously on differently oriented structures. Furthermore, these two earthquake swarms helped to delineate two sinistral Riedel shear zones (ENE-striking boundary structures represented in green in Fig. 1c). The largest seismic events in 1972 ($M_L > 4$) were located at the boundary (up to 2.6 km wide) between these Riedel shear zones (Fig. 1c).

A comprehensive paper by Khodayar et al. (2018)—which integrated remote sensing, field geology, and seismicity—showed that both the NRSZ and the SRSZ, located within the Reykjanes geothermal field, are populated by a series of minor and differently oriented structures and that the SRSZ block is more intensely fractured than the NRSZ block. The authors categorized these structures in terms of their orientation and kinematics (Fig. 1c): ENE-striking structures, which are subparallel to the NRSZ boundary, display sinistral sense of shear; N-striking to NNE-striking structures, which are mainly dextral strike-slip; NNE-striking to NE-striking structures, that bound for example two grabens at Haugur (Ha) and Mölvík (Mö), are mainly extensional faults and dikes intruding along NE-oriented fissures and faults; E-W structures, which, with significant uncertainty, are inferred to be dextral; and NW-striking to NNW-striking and WNW-striking structures, which are dextral (Fig. 1c; Khodayar et al., 2018). Dextral N-striking to NNE-striking structures in the SRSZ are difficult to observe at surface; hence, they are mainly mapped from earthquakes (Keiding et al., 2009). These are interpreted to represent a conjugate fault system together with the ENE-striking structures (Khodayar et al., 2018) and are observed to cut across NE-striking volcanic fissures and normal faults. Both these volcanic fissures and normal faults accommodate extension while N-S faults accommodate the transform component (Sæmundsson et al., 2020).

2.2. Preliminary fault model

In this section, we present how we extract a local fault model for our case study in which we incorporate measurements from wells and local geological studies. The study area is located at Sýrfell (Sý in Fig. 1c), approximately 2 km NE of the center of production (Fig. 1c), mainly in the NRSZ and partially across the boundary between the two shear zones (Fig. 1c). Structural information on this region relies on fault traces interpreted by Khodayar et al. (2018) and well data and televiewer interpretation from well RN-34 (see Supporting Material, Text S1). Although a detailed outcrop study of the area is missing, movements along the faults (or kinematics) are believed to mirror the overall structural pattern of Reykjanes. Furthermore, televiewer images from well RN-34 provide valuable information on orientation, infill, (mechanical) aperture, and kinematics of fractures intercepted by the well. A total of 404 N-striking and NE-striking fractures were interpreted in an unpublished report by Árnadóttir et al. (unpublished report, Supporting Material, Text S1). The dominating fractures (interpreted with high confidence) are subvertical (82°) and strike NNE (022°) on average. An apparent mechanical aperture larger than 19 mm was measured for a series of NNE-striking to NE-striking fractures (Fig. 1d).

Due to the opening of the NNE-striking to NE-striking fractures and their vicinity to feed points, Árnadóttir et al. (unpublished report, see Supporting Material, Text S1) assume that four of these fractures act as fluid pathways.

In an unpublished report, Khodayar et al. (Supporting Material, Text S2) suggested five preliminary fault models consisting of nine structures (labelled 1, 2, 3a, 3b, 4, 5, 6, 7 and 8 in the white rectangle in Fig. 1c), representing the starting point of our local fault model for the case study. Two of these faults have known dips (75° to NW) from the outcrop study; they did not intersect the well and are far from the seismic cloud (Fault 5 and 7 in Fig. 1c). These faults were therefore excluded from the fault

model. In the models, the remaining faults are believed to have constant dip, as do all of the faults in each model (70°, 75°, or 90°). The NW-oriented fault trace (Fault 6 in Fig. 1c), together with a similarly oriented lineament to the east (not shown in Fig. 1c), is, according to Khodayar et al. (2018), likely bounding the seismic cloud of the 2015 swarm (including events occurring on 12 December 2014). This structure is unfavorably oriented to slip since it is orthogonal to the σ_1 axis (as discussed in Sections 2.3 and 2.4). We assume that it has limited impact on flow. Therefore, it has also been excluded from the fault model.

2.3. Revised fault model based on the analysis of induced seismicity

We now incorporate observations from seismicity occurring in Reykjanes Peninsula to refine the local fault model geometry. The lack of clear reflectors and large impedance contrasts impair the value of conventional active seismic methods and make difficult the identification of geological structures. Hence, locations of induced and natural seismicity can be used as an alternative approach for the identification of faults. One benefit of analyzing induced seismicity is that active faults will be identified. This comes as additional information to all mapped faults, which can be locked and impermeable, and the seismicity can also identify smaller, previously unmapped faults. Active faults are likely to have relatively large aperture and permeability and are thus suitable for geothermal exploration. Since seismicity was induced during fluid injection, we use the respective locations of the seismic events to further constrain the geometry of the local fault model.

The seismicity used for refining the fault model occurred within the Reykjanes Peninsula and is linked to the continuous fluid injections in RN-34 from 20 May to 13 August 2015. It was recorded by both a permanent and a temporary seismic network (Fig. 1b). The permanent network (PS) was run until 2018 by the Iceland Geosurvey (ISOR) on behalf of HS-Orka and was composed of eight short-period sensors mostly located above the geothermal reservoir on the SW part of the Reykjanes Peninsula (Weemstra et al., 2016). A temporary network (TS) with 20 broadband and 10 short–period sensors covering the entire Reykjanes Peninsula was installed as part of the European Project IMAGE and took recordings from March 2014 to August 2015 (Blanck et al., 2020; Jousset et al., 2016; Jousset et al., 2020; Supporting Material, Table S10). However, both networks suffered from temporary data gaps. The variety of sensor types and the short (0.8 km) and long (35 km) interstation distances increase the network resolution and the capability of recording close and far events. Induced events have been observed at Reykjanes since the start of the geothermal activity (Blanck et al., 2020; Flovenz et al., 2015; Guðnason, 2014).

To further improve the estimated fault model, we extract event locations and focal mechanisms from the clouds of weaker seismic events and from individual earthquakes. Here, the relative event locations within a seismic cloud can reveal the general fracture orientation (strike and dip), a.k.a. seismic lineation, and the focal mechanisms can be determined from larger individual events to constrain the orientation of causative slipping fractures.

From the 3D locations of the events, we extracted the principal axes of the best-fitting ellipsoid containing the event clouds. Then, we apply a plane fitting method based on the computation of the covariance matrix of the events' point cloud to extract strike and dip and compare this geometry to the fault plane geometry, which already is present in the model.

To determine fault plane slipping during a seismic event, focal mechanisms are computed. These graphical representations provide two orthogonal fault plane solutions, of which only one is the correct active or causative fault. Discriminating between the two solutions often relies on other information (e.g., distribution in space of the focal mechanisms,

fault mapped at surface, etc.). Constraining focal mechanisms of small events can be more challenging when the amplitudes of first arrivals are small and the noise levels are high, as is often the case when investigating microseismic events with surface networks.

2.3.1. Interpretation of seismicity

Here, we use the seismic events occurring from the start of continuous injection within RN-34, 20 May 2015, to the removal of the temporary seismic network, 13 August 2015 (wider yellow region in Fig. 2a). Automatic event detection was applied on continuously recorded seismic data and led to ~6500 seismic event detections. For about 2000 of these detections, phase onsets for direct P- and S-waves were automatically determined following an aggregated template methodology (Duboeuf et al., 2021). All determined phases were subsequently quality controlled visually. The entire set of picked events was located using the Icelandic 1-D layer velocity model South Iceland Lowland (SIL, Bjarnason et al., 1993) and a differential evolution algorithm (Storn & Price, 1997; Wuestefeld et al., 2018). The relative location accuracy was increased using a Double-Difference relative location method (Waldhauser, 2000) (Fig. 1c). A detailed analysis of seismic processing methods can be found in Duboeuf et al. (2021). Most of the individual event location uncertainties are in the order of 100 to 300 m, based on the formal computation of the covariance matrix. The uncertainties are in average larger with depth as compared to the spatial direction, primarily due to the network configuration (e.g. Supporting Material, Table S8). We did not re-evaluate the location uncertainties based on residuals and e.g. a bootstrap approach after re-location, but we see a qualitatively improved structure in the event locations. Seismic events were further grouped into several families based on waveform similarities and event locations. One group of 687 events was likely related to a fluid injection in well RN-34 (white events in Fig. 1c). The moment magnitudes (M_w) of these events range from about 0.8 to 3 and were determined by fitting a Brune model (Brune, 1970) to the observed seismic spectra.

Furthermore, seven time periods display a distinct increase in the seismic activity that surpasses the daily average (> 10 events/day); these are numbered 1 to 7 in Fig. 2a. We refer to this spatially and temporally limited increase in seismic activity as "bursts." Bursts occur within short time intervals (from a few hours to one week) and are concentrated in relatively small spatial regions, supporting the idea that they might be caused by slip on the same structure.

In order to test this hypothesis that bursts could occur on the same structure, we fitted planes to each of the bursts (1 to 7 in Fig. 2a and Fig. S1, Supporting Material). The results suggest that six out of seven fitting planes are ENE-striking (ellipses in Fig. 2b and Fig. S1, Supporting Material), which is supporting that they could have occurred on the same structure. Strike and dip of the planes are reported in Fig. 2b, showing larger variability in the dip than the strike. This is likely attributable to greater uncertainty in the depth of these events due to the lack of sensors at depth, resulting in poorly constrained dip of the faults. Bursts with a larger number of events (numbers 1 and 4 with 94 and 325 events, respectively) suggest steep (87° and 82°) fault planes. The closest similarly oriented structure to these fitting planes is Fault 4 (Fig. 1c). However, because of the proximity (approx. 200 m, which is lower than location error) of the two other similarly oriented structures (Faults 3a and 3b, Fig. 1c), we cannot rule out that the causative structure could also be one of those.

As focal mechanisms allow for determination of fault plane geometry and slip, we computed 170 focal mechanisms from P-wave first motion polarities, for the three months period. The focal mechanism inversion is based on Kwiatek and Ben-Zion, (2013) and further modified by Langet et al. (2020) to include multiple weighting schemes and quality control plots. Additional weights were introduced because this kind of inversion otherwise often results in multiple, equally well constrained solutions. In this modified inversion, the quality and impulsiveness of the individual polarities as well as the distance of the individual observation to a

nodal plane are weighted. The number of observations, azimuthal coverage, potential number of polarity flips, and quality of the observations are used to finally describe the quality of the best solution. The magnitude of these events is between M_w 1.14 and 2.62. The focal mechanism solutions indicate that the prevailing faulting types are strike-slip (52%) with near-vertical focal planes, normal (19%), and normal oblique (15%). Purely thrust (5%) and strike-slip with thrust component (2%) fault motions have also been identified. Finally, 7% of the determined focal mechanisms seemed to represent some percentage of non-double-couple components, which might be expected in an injection area (Julian et al., 1998; Zhao et al., 2014), however, more elaborate analysis will be required to secure this observation. In the inset in Fig. 2b, a selected number of focal mechanisms of high quality ($>$99%) are superimposed on the planes that best-fit the bursts. The quality of these focal mechanisms is normalized and based on the number of solutions, observations, and misfits. However, the locations of these focal mechanisms do not clearly align along one specific structure. The two focal mechanisms that can best explain the computed stress indicate two possible fault plane solutions: (1) sinistral 075°/83° or dextral 168°/67° and (2) dextral 190°/71° or sinistral 90°/75° (Fig. 2c). Although the strike variation between the fault plane solutions of the two principal focal mechanisms is only 25°, we analyze these results separately and compare them with fitted fault planes and fault traces. The ENE-striking focal plane (075°/83°) of the first principal focal mechanism has a similar orientation to the fitted planes of the bursts. It is also consistent in terms of both orientation and kinematics (sinistral strike-slip) with fault numbers 3a, 3b, and 4 of the fault model. Associating the second principal focal mechanism to a causative structure in the fault model is more complicated and not unique. The N-striking dextral strike-slip focal plane (190°/71°) is, to a certain extent, similar to Fault 2 (Fig. 1c); similarly oriented faults are recognized as responsible for earthquakes on the Reykjanes Peninsula (see, e. g., Keiding et al., 2009). Although the other focal plane (90°/75°) of this focal mechanism has the same orientation as structure number 8, this fault is likely to be dextral (Khodayar et al., unpublished report, Supporting Material, Table S3) and therefore does not fit with the focal mechanism solution. N-striking and ENE-striking planes could represent conjugate fault planes that have been observed elsewhere in Iceland (Khodayar et al., 2018). Based on fractures intercepted by the well and on computed focal mechanisms, the faults in the model are interpreted to be vertical.

2.3.2. Final revised fault model

The joint geological and seismic data analysis presented in the previous section allows us to define the final fault model. The final model consists of six vertical faults: one N-striking to NNE-striking structure (028°), Fault 2; one NNE-striking to NE-striking structure (034°), Fault 1; three ENE-striking structures (between 058° and 063°), Faults 3a, 3b, and 4; and one E-striking structure (strike of 100°), Fault 8 (Fig. 3, left. Table 1). ENE-oriented fault traces (Faults 3a, 3b, and 4 in Fig. 1c) coincide with this interpreted surface expression of the boundary between the northern and the southern Riedel Shear Zones. They show a right-stepping en échelon arrangement similar to what has been observed elsewhere on the Reykjanes peninsula, typical of sinistral strike-slip kinematics (see Fig. 1c). Uncertainties exist on the cross-cutting relationships (e.g., terminations or abutments) between the different fault sets (e.g., ENE-striking and NNE-striking to NE-striking), and interpretation in Khodayar et al. (2018) (Section 2.1) did not match what was previously presented in a fault model scenario by Khodayar et al. (unpublished report, Supporting Material, Text S2). For example, in the former, ENE-striking faults are believed to cut NNE-striking to NE-striking volcanic fissure and normal faults, while in the latter, Fault 3b (ENE-striking) terminates on Fault 2 (NNE-striking to NE-striking). For this reason, cross-cutting relationships are not included in our final fault model.
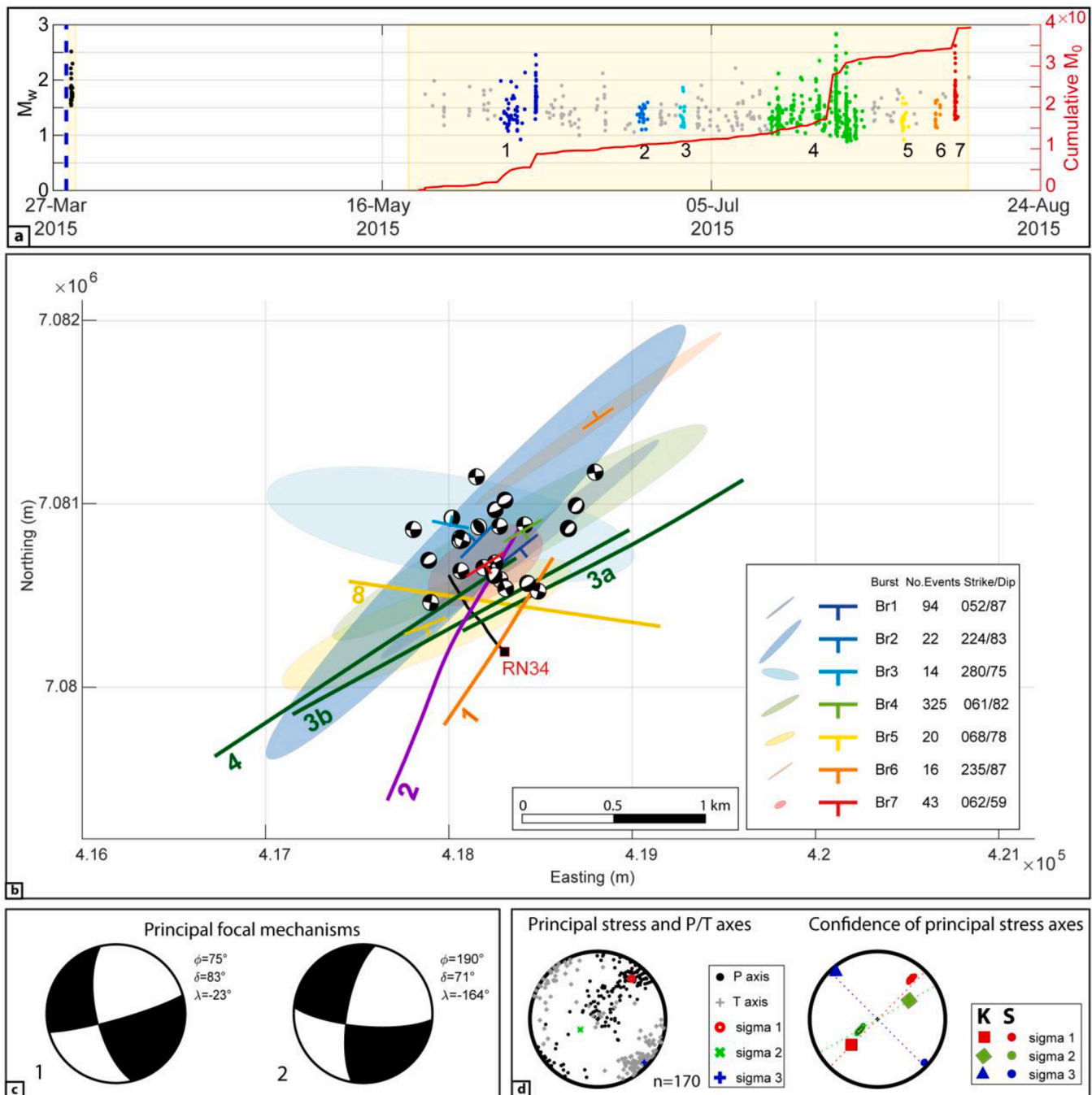
Fig. 2. (a) Time vs. moment magnitude (M_w) plot showing seismicity at well RN-34. White regions represent periods where no data are available. Seven periods of increased seismicity for the period between 20 May and 13 August 2015 are shown as colored dots, numbered from 1 to 7. Cumulative seismic moment (M_0) during the same period is also shown (red curve). The blue dashed line illustrates the date of the stimulation; more details on the injection history are shown in Fig. 4b and c. (b) Fitted planes (ellipse and strike/dip symbol in the same color scheme as used in Fig. 2a) to each burst and well-resolved focal mechanisms occurring in the same region. Ellipses are reduced in size (50%) for visualization purposes. Well RN-34 is also shown (grey). (c) Principal focal mechanisms as derived from the stress inversion following Vavryčuk (2015) showing strike–slip kinematics, with Φ denoting strike, δ dip, and λ rake. (d) Left: principal stress and P/T (Pressure or compression/Tension) axes; Right: confidence of principal stress axes inverted from 170 focal mechanisms (S) and stress orientation from Keiding et al. (2009) (K). Note that P/T axes correspond to σ_1 (sigma 1) and σ_3 (sigma 3) axes. (For interpretation of the references to color in this figure legend, the reader is referred to the web version of this article.)

2.4. Stress state

The stress state determines a mechanical boundary condition for the 3D hydro-mechanical model. Thus, information on the stress (magnitude and orientation) is required and can be inferred from focal mechanism inversion as long as the seismic events are large enough and do not represent local stress field heterogeneities (Cornet et al. 2007). Hereafter, we will compare the stress state reported in literature to the one we obtained from the 170 focal mechanism inversion (see Fig. 2d).

Keiding et al. (2009) derived the direction of the stress from focal mechanism inversion for the period 1997–2006 and then compared it to strain rates from GPS data for different regions in Iceland. Furthermore,
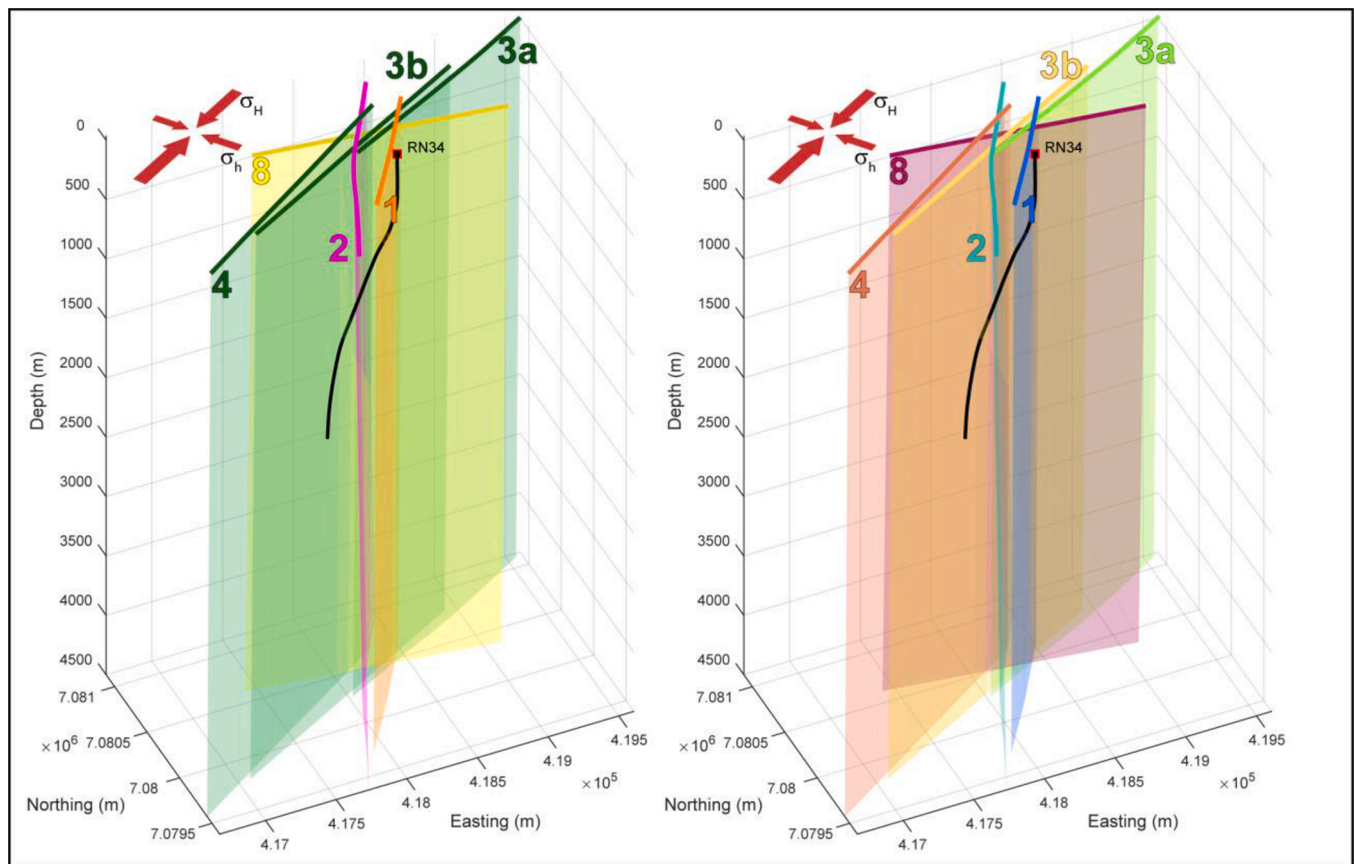
Fig. 3. Fault model consisting of six faults. Left: Color scheme based on orientation and kinematics following unpublished work by Khodayar et al. (unpublished report, Supporting Material, Text S2). Right: Color scheme used for visualization of simulation results (see Section 5), with different colors for each fault. Well location (square) and path (black line) are also shown. (For interpretation of the references to color in this figure legend, the reader is referred to the web version of this article.)

Table 1

Numbered faults planes identified from surface used to build the five fault models. Data taken from Khodayar et al. (unpublished report ÍSOR-2015/16; see Supporting Material, Introduction, point 1b). * = uncertain.

Index	Strike direction	Strike [°]	Dip [°]	Motion as deduced from surface
1	NE-SW	034	90	Open *
2	NNE-SSW	028	90	*
3a	ENE-WSW	063	90	Sinistral
3b	ENE-WSW	061	90	Sinistral
4	ENE-WSW	058	90	Sinistral
8	E-W	100	90	Seismic lineation, Dextral *

maximum horizontal stress derived from 15 orientation breakouts in RN-34 are reported in Ziegler et al. (2016). The orientation for the western Reykjanes peninsula (extrapolated from Keiding et al., 2009, Fig. 7) is 220°/50° for the maximum principal stress axis σ_1, 064°/40° for the intermediate principal stress axis σ_2, and 323°/10° for the minimum stress axis σ_3. However, eastwards, the stress orientation changes toward the strike-slip regime of the SISZ. A model that advocated the permutation of two of the principal stress axes σ_1 and σ_2 was initially used to explain oblique rifting, supported by the alternation of extension and strike-slip episodes and tectono-magmatic activity. However, the observed coexistence of normal, strike-slip, and oblique fault ruptures during both the swarm in 1972 and in 2013 (Khodayar et al., 2018; Klein et al., 1977) suggests a transtensional regime (intermediate case between normal and strike-slip regimes) in which differently oriented structures accommodate deformation.

For the 170 focal mechanisms derived in this study, we conducted a stress field inversion based on the method of Vavryčuk (2014); our resulting principal stress orientations are σ_1 (040° ± 5°)/23°, σ_2 (230± 10°)/66°, and σ_3 (140° ± 10°)/7°. The orientation of σ_1 is consistent with the strike of the maximum horizontal stress (034°) derived from breakouts in RN-34 (Ziegler et al., 2016). Note that the orientation of σ_3 is almost identical to that predicted by Keiding et al. (2009) (Fig. 2c, right), while σ_1 and σ_2 show the same trends but plunge on opposite quadrants. In addition, a series of stress inversion tests with varying friction coefficient shows that the most robust stress state is obtained for a friction coefficient of 0.4. This value is quite low compared to the 0.6–0.8 usually used (Byerlee, 1978). However, such a value has previously been observed when faults are partially filled with clays or low-friction minerals (Janecke & Evans, 1988; Kanji, 1974). In high temperatures, such as those present in the study region and relevant faults, decreased friction coefficients with temperature have been observed (e.g., by Di Toro et al., 2011).

Although information on stress orientation exists for the Reykjanes peninsula, direct measurements or estimates of stress magnitudes are lacking. Scenarios of four stress cases (corresponding to Andersonian's stress orientation plus a transtensional case) were accounted for by Peter-Borie et al. (2018) in their modeling of drilling effects and fracture initiation caused by stimulation of well RN-15/IDDP2 (circa 1.5 km SW of the study area). In their study, vertical stress magnitude was estimated according to gravitational loading (134 MPa at a depth of 4560 m), and horizontal stress magnitudes were extrapolated from the stress state modelled by Batir et al. (2012) and Peter-Borie et al. (2018). The numerical model of stress was then compared to observations from well images suggesting that the strike-slip fault scenario and, to a lesser extent, the transtensional regime scenario predicted the breakouts more accurately. Based on the above discussion, in the simulations reported in

Section 5, the maximum and minimum stresses are both assumed to be in the horizontal plane. Based on the work by Batir et al. (2012) and Peter-Borie et al. (2018), the maximum and minimum horizontal stress magnitudes are chosen as 1.5 times and 0.45 times the vertical, lithostatic stress, respectively, with the maximum principal stress oriented in a NE-SW direction (see Fig. 2d).

To summarize, from the geological and seismic analyses, a final, revised fault network geometry has been established and mechanical boundary conditions for the 3D hydro-mechanical model has been defined.

3. The 29 March 2015 RN-34 fall-off test and cyclic well stimulation

In this study, we aim to model the hydraulic stimulation of the well RN-34 29 March 2015 and its effects in term of fault deformation and hydro-mechanical process. This section describes available static measurements from well RN-34 as well as data from the 29 March 2015 testing and stimulation of the well. The operation consisted of two stages: a fall-off test followed by cyclic stimulation. For both stages, pressure and volume data are available, as is information from seismic monitoring.

3.1. Static and time-dependent well data

RN-34 had been drilled to a depth of 2667 m on 27 March 2015 (Supporting Material, Text S3)[1]. Following rinsing of the well, a televiewer survey was conducted. Televiewer imaging indicated several possible feed points along the wellbore, with the main feed points most likely in the depth interval 2300–2600 m (Supporting Material, Text S1).

Testing of the well commenced on 29 March 2015 with a fall-off test followed by hydraulic stimulation. The fall-off test consisted of constant injection at a rate of 43 L/s from 07:15 to 09:50, followed by an abrupt shut-in. The pressure was monitored in the well at a depth of 1400 m, that is, about 1000 m above the assumed leakage points from the well into the rock. Recording of data (shown in Fig. 4b; see also Supporting Material, Text S4 and Tables S5-7) started about 30 minutes before the shut-in and continued until 1.5 h after shut-in (recording period 09:20–11:15). As can be seen from Fig. 4b, the pressure was stable toward the end of the injection period and then decreased significantly after shut-in. The pressure drop between plateaus during and after injection was about 2.8 MPa.

The following well stimulation was performed from 12:00 to 22:00 with a cyclic injection pattern with injection rates of 100 L/s applied for 1h, followed by rates of 20 L/s for periods of 20–30 min (Supporting Material, Text S3). In the stimulations reported in Section 5, the durations of low injection rates were set to 30 min (see also the illustration in Fig. 4c).

3.2. Induced seismic events

The seismicity was monitored by the PS and TS networks (see Section 2.3). No seismicity was observed during the fall-off test. A sequence of 33 seismic events was observed in the period from 16:00 to 22:00, four hours after the stimulation characterized by the highest injection rate (100 L/s) started. The events are mainly located east of the injection point and north of Fault 8 (Fig. 4a), consistent with observations during the three months of injection (Fig. 1c). As the pressure and injection flux were not recorded at the well during the stimulation (Fig. 4c), we could not link the triggered seismicity to any potential change in well pressure. However, the injection rates were higher than during the fall-off test. The proximity of the seismic events to the injection point (Fig. 4a and

4c) and the fact that the events occurred during the stimulation phase suggest that they were induced by the fluid injection. The moment magnitudes vary from 1.5 to 2.5, which is within the range of the seismicity for the three months of analysis (M_w 0.8 to 3). However, the seismicity shows neither clear pattern (for example in terms of the spatial, temporal and magnitude distribution of events) nor correlation between locations and event occurrence time (Fig. 4a).

The two principal focal mechanisms computed for 29 March 2015 (Fig. 4d) show similar orientation and motion as the two principal focal mechanisms identified through the three-month period (20 May to 13 August 2015) of seismic analysis shown in Section 2 (Fig. 2b). Regarding the first principal focal mechanisms for both periods (29 March 2015 and the three-month period), one of the fault plane solutions is an ENE-striking plane with similar strike (258° vs. 075°) and dip (83° vs. 85°) but opposite dip-direction (north vs. south). The other fault plane solution is a N-striking plane with similar strike (165° vs. 168°) and dip-direction but slightly different dip (85° vs. 72°). With regards to the second principal focal mechanisms for both periods, the N-striking plane solutions have a similar strike (190° vs. 189°), dip (76° vs. 71°), and dip-direction. These differences are not significant with respect to the relatively small number of events analyzed here. We hence assume that reactivated structures during the stimulation on 29 March 2015 are likely the same as the structures reactivated during the latter three months of continuous injection.

To summarize, the sequence of microseismic events during the short-term injection test on 29 March appears to be representative for the period from 20 May to 13 August in terms of spatial location, magnitude, focal mechanisms, and reactivated structures. Based on these observations, we propose that the local fault model can be representative for both, the short-term fluid injection and the longer injection period. In addition, this suggests to use vertical fractures for the modeling.

4. Hydro-mechanical simulation tool

In this section, we introduce a hydro-mechanical reservoir model to conceptualize the observations presented in Sections 2 and 3 and to simulate the stimulation of well RN-34 on 29 March 2015, with fluid injection into a faulted reservoir as well as the mechanical response of the faults and the host rock to the fluid injection. As the injection period of the stimulation is short, with relatively low injection rates, thermal stimulation effects are not considered since the injected fluids will quickly heat up and any significant thermal stresses will be local to the injection well on a scale which is not considered in the current study (Ghassemi et al., 2005; Grant et al., 2013; Stefansson et al., 2020).

One main challenge in the numerical modeling of processes in faulted rocks is the large aspect ratio of faults and heterogeneity between faults and host rock. As the dominant physical processes in the faults are either different from those in the host rock or have substantially different characteristics, an upscaled representation that integrates host rock and faults into a continuous medium lead to models with poor accuracy. In particular, modeling of fracture reactivation and slip requires accounting for the deformation of the faults and the host rock and the coupling between them. How to incorporate this into a simulation model depends on whether the faults are resolved by the computational grid or not. Several studies have avoided resolving the fractures by applying subgrid-scale models to represent fracture-matrix interactions (Izadi & Elsworth, 2014; Norbeck et al., 2016; Rutqvist et al., 2015). Herein, we pursue a different and more accurate approach, based on Discrete Fracture Matrix (DFM) principles (Berre et al., 2019), with the major faults explicitly represented in the computational grid. To avoid resolving the domain across the relatively thin faults, the faults are represented as lower-dimensional objects. The explicit representation gives transparent couplings of processes in host rock, fault network, and on the fault walls and, moreover, allows for high resolution of the sliding process. The effect of small-scale fractures, which are not explicitly represented, may be approximated by upscaling into matrix parameters.

---

[1] Drilling was completed on 2 April 2015 at the final depth of 2695 m (Supporting Material, Text S3).
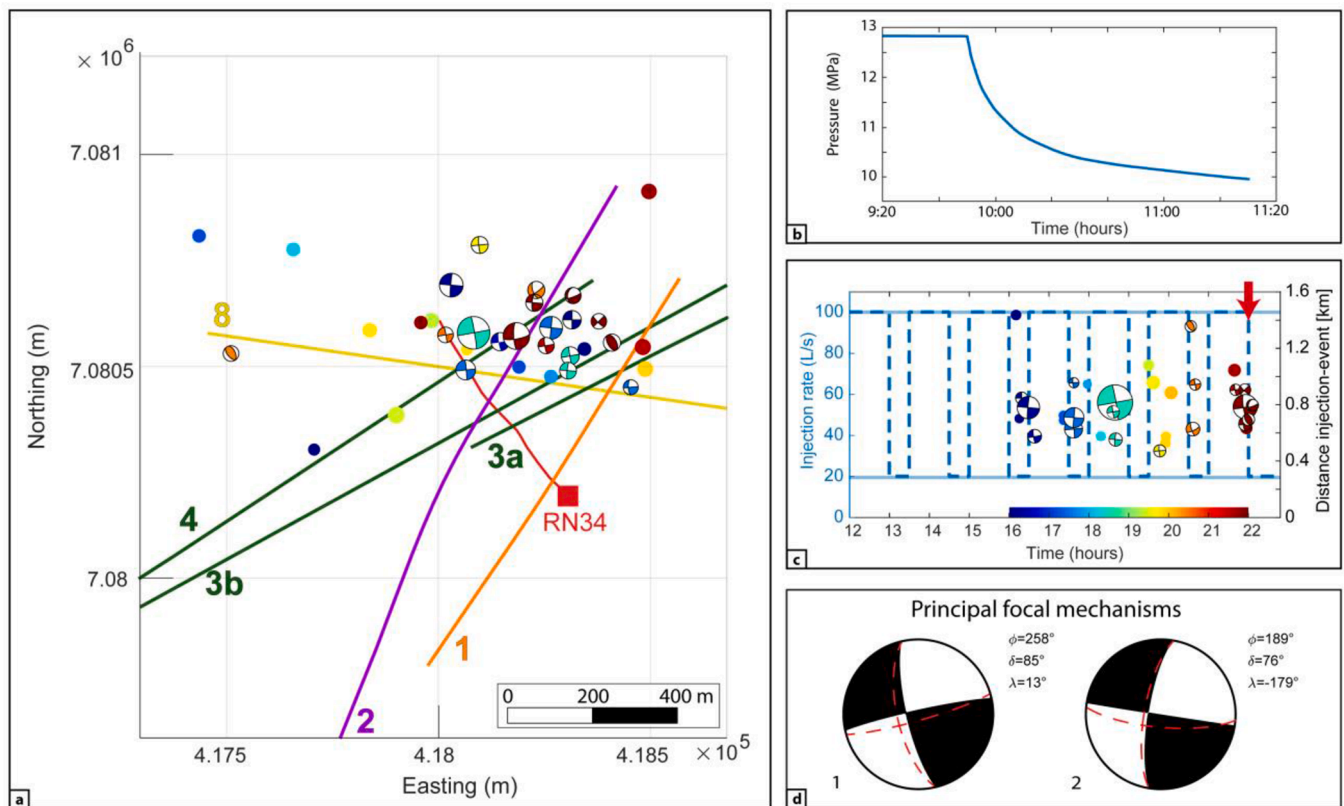
Fig. 4. RN-34 injection test on 29 March 2015, seismic event occurrence, magnitude, and focal mechanisms. (a) Seismic event locations in map view, fault traces, and RN-34 well location. Colored dots represent seismic events; focal mechanisms are shown where determinable. The color scale applied to seismic events range in time from 16:00 (blue) to 22:00 (red); see subFig. (c). (b) Pressure evolution at the monitoring point during the fall-off test. (c) Injection rate (stippled line) and seismicity vs time, including the distance of a seismic event to the injection point. The applied injection rate altered between 20 and 100 L/s, with intervals of 20–30 min intervals (Note: Detailed injection data not available). Dot and beach ball sizes are scaled by moment magnitude M_w 1.51 to 2.51. Red arrow corresponds to stimulation end. (d) Principal focal mechanisms showing strike-slip kinematics. Red dashes show the principal focal planes from the three months of injection. (For interpretation of the references to color in this figure legend, the reader is referred to the web version of this article.)

While variants of DFM models have previously been applied to study shear stimulation of fault networks in geothermal reservoirs (Kolditz & Clauser, 1998; Sun et al., 2017; Ucar et al., 2017; Ucar et al., 2018a; Berre et al., 2020), this is, to the best of our knowledge, the first attempt at applying DFM models to simulation of coupled flow, mechanics, and fracture reactivation and slip for a case study from an actual geothermal reservoir.

The processes included in our simulation model are summarized as follows: The host rock is considered a poroelastic medium with a linear isotropic relation between stress and displacement. Fluid flow in the rock matrix and the fault network is modeled by Darcy's law. The deformation of the fault is modeled as a frictional contact problem between the fault walls: the fault can be open, in contact but sticking, or in contact and sliding. The latter is characterized by a jump in the tangential displacement of two opposing fault walls. This model is similar to previous models for poroelastic media with fractures modeled by contact mechanics considered recently (Berge et al., 2020; Gallya-mov et al., 2018; Garipov et al., 2016; Garipov & Hui, 2019; Keilegavlen et al., 2021; Stefansson et al., 2020). Due to the limited data available to parameterize the model, the model applies only a constant friction coefficient and does not account for permeability enhancement due to shear dilation, although this could have been included (e.g., as by Stefansson et al., 2020). The full set of governing equations can be found in the appendix.

The computational grid is constructed to conform to the explicitly represented faults. Faces on a fault surfaces are split, and lower-dimensional cells are inserted between the split faces (see Fig. 5). The degrees of freedom in the simulation model are specified as illustrated in

Fig. 5: In the matrix grid, displacement and pressure are represented as cell-centered variables. Additional displacement degrees of freedom are placed on the faces on the fault surfaces. Finally, in the fault grid, fluid pressure and contact force (both normal and tangential) are represented by cell center values.

The simulations are performed using the open-source simulator PorePy, described in Keilegavlen et al. (2021), and applying the following combination of discretization schemes: Poroelastic deformation of the matrix is discretized by the Multipoint Stress Approximation (Nordbotten, 2016; Nordbotten and Keilegavlen, 2021; Ucar et al., 2018b). Flow in matrix and faults is discretized by a Multipoint Flux Approximation (Aavatsmark, 2002), with the fluid flow between matrix and faults considered within the framework presented by Nordbotten et al. (2019). The simulation framework does not include a well-model but represents injection in a simplified manner by point sources in cells. The contact mechanics formulation for fault deformation uses a semi-smooth Newton approach as described by Berge et al. (2020) and Hüeber et al. (2008).

5. Simulation results: cyclic stimulation of RN-34 29 March 2015

Our goal in this section is to present simulations of the 29 March 2015 stimulation of RN-34 and to compare the results with the analysis of seismic events as described in Section 3. To that end, a simulation model is constructed based on the geological information above. Runscripts for the simulations are available in (Keilegavlen & Stefansson, 2020).
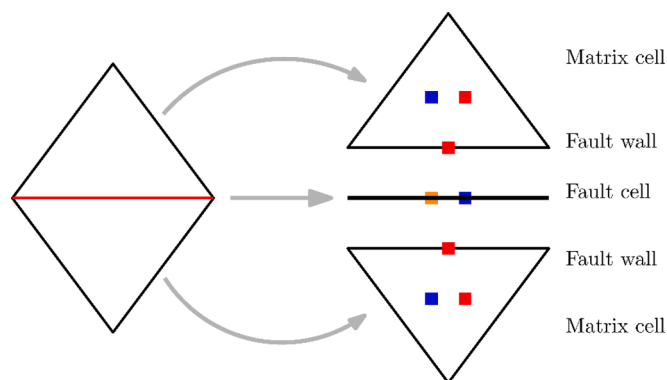
Fig. 5. Illustration of conceptual model and degrees of freedom, shown in 2D for simplicity. Left: A DFM conceptual model, where the fault (red line) is represented as a lower-dimensional object. Right: Degrees of freedom: The deformation (red) is represented in matrix cells and on fault walls, fluid pressure (blue) in matrix and fault, and contact force (orange) in the fault. (For interpretation of the references to color in this figure legend, the reader is referred to the web version of this article.)

5.1. Construction of simulation model

The geometry of the fault network is taken as described in Section 2, and the full simulation domain is specified by a bounding box with a horizontal extent of 10 × 10 km. In the vertical direction, the simulation domain is set to 4 km. The faults are represented as being linear in the horizontal direction and assumed to be vertical and extending to the top and bottom boundaries of the domain (Fig. 6). The simulation grid is created by first meshing the 2D horizontal domain with 1702 cells and then vertically extruding the grid with nine layers of non-uniform thickness, so that the zone near the injection has the highest grid resolution. The simulation grid for the matrix is illustrated in Fig. 6.

The elastic moduli of the rock matrix are defined according to the seismic velocities of the rock, accounting for vertical variations of the rock properties; the assigned values are based on those reported by Bodvarsson et al. (1996) and given in the Supporting Material, Table S9.

In accordance with Section 2.4, the stress is assumed to be in a strike-slip regime, with the maximum and minimum principal stress directions both in the horizontal plane. These values are boundary conditions for the momentum conservation in the simulation model. The static friction coefficient on fracture surfaces was set to 0.4 in accordance with the analysis presented in Section 2.4. The Biot coefficient was set to 0.8 and rock density to 3000 kg/m^3.

The parameters used in the flow model are fault and matrix permeability, matrix porosity, and the location of the feed points from the injection well into the formation. All of these parameters are both critical for the simulated formation response to the stimulation and highly uncertain.

The feed points are assumed to be toward the bottom of the well (Section 3.1) and associated with highly permeable faults, moreover, all feed points lie on the same side of the potentially blocking Fault 8. For simplicity, the simulation model implements the feed point in the fault cell closest to the well at a depth of 2500 m. In practice, this places the feed point in Fault 4.

The permeability values for the faults and matrix are reported in Table 2. The values are homogeneous in the matrix and for each of the faults and were held constant during the simulations. High permeabilities are assumed for Faults 1 to 4. The permeability of Fault 8 is considered as unknown prior to the simulation study. Its orientation relative to the regional stress field indicates it may have very low permeability, moreover, the seismic events are mainly located to the north of this fault (see Fig. 4a). Based on this, three scenarios were defined, with Fault 8 defined as permeable (Case A), as having permeability equal to that of the matrix (Case B), and as sealing (Case C). For each of these scenarios, the matrix permeabilities were tuned to reproduce the pressure drop measured in the leak-off test run on the morning of 29 March 2015. In this calibration, mechanical effects were ignored. While we acknowledge the simplicity of this approach, a richer parametrization and more elaborate calibration is not warranted due to the scarcity of data. Fluid properties are given in Table S9, Supporting Material. The flow simulation model is complemented by hydrostatic conditions at the lateral and upper boundaries and no-flow conditions at the bottom.

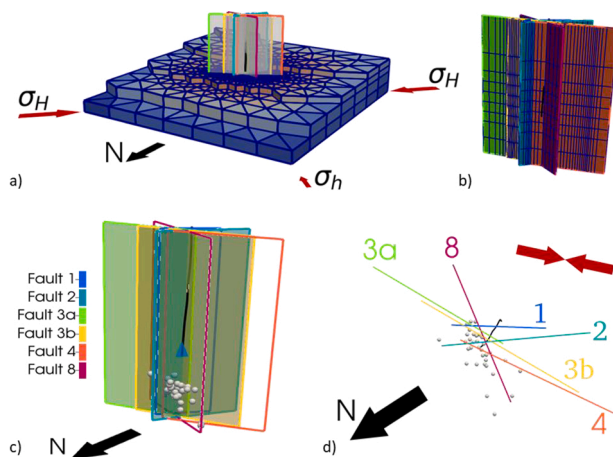The hydro-mechanical simulation model is initialized by simulating

Fig. 6. (a) The 3D simulation grid, split to expose the fractures. The coloring of the matrix cells shows the perturbation in pressure from the initial state for Case C. (b) The simulation grid in the fault network, the faults extend to the bottom of the simulation domain. (c) The fault network with the color coding used for all visualization of simulation results, the well path (black), the approximate location of the injection point (blue triangle), and the seismic observations (spheres). The orientation is chosen for optimal readability of the simulation results (Figs. 7–9). (d) The fault network, well path, and seismic observations seen from above. The direction of maximum horizontal stress is indicated by red arrows. (For interpretation of the references to color in this figure legend, the reader is referred to the web version of this article.)

a scenario with no injection until steady state is reached. As we have no information on the stress history of the reservoir, the stress boundary conditions in this initialization are taken as the current background stress field. Hence, the initial stress state of the faults in the simulation model may deviate from that of the reservoir, and fractures are critically stressed where slip has occurred. In the initialization, Faults 2 to 4 all undergo slip with a magnitude of centimeters. Thereafter, the cyclic stimulation pattern described in Section 3 is simulated with a time step of 15 minutes, which was found to be suitable to properly account for the 30 minutes injection steps. In the discussion that follows, we mainly focus on the fault network.

5.2. Simulation results

We first consider the initial slip tendency, defined as the ratio of tangential to normal forces on the fault surfaces (e.g. Moeck et al. 2009). As can be seen in Fig. 7, the slip tendencies at the start of the stimulation for significant parts of Faults 2, 3a, and 3b attain the maximum possible value (equal to a fault friction coefficient of 0.4) and are thus critically stressed. Except for the tip of Fault 4, Faults 1, 4, and 8 have lower values. The slip tendencies along the faults undergo only minor changes during the stimulation. Hence, Faults 1, 4, and 8 remain primarily un-critically stressed, and we report pressure profiles and tangential sliding for Faults 2, 3a, and 3b only. Of these, Fault 2 is connected to the injection point through the fault network without going through the potentially blocking Fault 8, while Faults 3a and 3b are favorably oriented with respect to the background stress field.

Fig. 8 depicts pressure perturbations from the steady state at the end of the stimulation period (red arrows in Fig. 4c). For Case A, the pressure perturbation is relatively high due to its lower matrix permeability, and pressure is diffused throughout the fracture network. In contrast, for Case C, the pressure perturbation is much lower and, to a large degree, localized in the part of Fault 2 that is on the same side of the sealing fault as the injection point. For the intermediate Case B, there is substantial pressure diffusion in the fault network due to the lack of a seal.

The slip along Faults 2, 3a, and 3b is shown in Fig. 9. The slip profile is remarkably similar for the three cases, although the magnitudes of slip differ between them; the largest magnitudes were observed for Case A, which also has the most pronounced pressure diffusion in the fault network. The slip along Fault 2 for Case C is divided into a region close to the injection point and a region on the far (south) side of Fault 8. A similar division is not present in Cases A and B. Thus, for Case C it seems reasonable that the slip on the north side of Fault 8 is directly caused by fluid injection, while slip on the south side can be attributed to changes in the poroelastic stress in the surrounding rock matrix.

6. Discussion

The improved understanding of the hydro-mechanical processes provided by the simulation results further advances interpretations of the induced seismicity.

6.1. Active fault identification

During the cyclic stimulation of RN34 on 29 March 2015, 33 seismic

events were observed. The events were mainly located east of the injection point, north of Fault 8, and below the bottom of the well.

For the given simulation model, the highest slips are predicted for Faults 2, 3a, and 3b, suggesting those are the main active faults. This underlines how modeling is able to discriminate slip on close-by and similarly oriented faults (e.g., 3a, 3b, and 4). In this case study, such a discrimination cannot be done using the seismicity location as location uncertainties are larger than the distance between the faults. Regions of main simulated slip along these faults are consistent with observed seismicity during stimulation of RN-34. Seismic analysis (Section 2.3) of the data from the latter three-month injection period, 20 May to 13 August 2015, identifies the ENE-striking faults (Faults 3a, 3b, and 4) as most likely being the active faults. Simulation results show that while Faults 3a and 3b are active, Fault 4, located in the shadow of the nearby active faults, is mainly inactive. However, Fault 4 has some slip and a high slip tendency, in particular near its south-west tip. Shadow effects can also be seen on Fault 2, which has less slip in the region close to where it is intersected by Faults 3a and 3b. Hence, when the location of seismicity is uncertain in regions of nearby and similarly oriented faults, modeling allows us to discriminate on which of the faults slip is more likely to occur.

6.2. Coupled hydro-mechanical effects

The 3D hydromechanical model predicted the largest pressure increase for Fault 2. However, Fault 2 is not the most likely active fault identified by the seismic analysis (Section 2.3). As the seismic events do not follow any diffusion law in this case study (RT plot, Fig. 4.c), seismic events observed nearby the stimulated well might not be induced by fluid overpressure. In the simulation results, large regions of Faults 2, 3a, and 3b are initially critically stressed. Wynants-Morel et al. 2020 showed that faults initially close to failure favor rupture and seismicity outside of the pressurized area. This is in agreement with the observed seismic locations, which are outside of the predicted highest pressurized zone. Consequently, the jointly analyzed results from modelling and seismic analysis may suggest that the injection induced seismicity should not be limited to the volume of highest pressurization and may already be preceding this volume (De Barros et al. 2019, Cappa et al. 2019, Wynants-Morel et al. 2020).

The simulations also suggest fault slip in regions further away from the observed cloud of seismicity. At first, this may point towards a disagreement between numerically modelled slip, and slip observed through seismic data interpretation. However, slip on faults may also occur at lower slip velocities, and in that case, no or significantly less seismic energy will be radiated by the slow-slipping event into the rock. This kind of slip is often referred to as aseismic deformation. Evidence of aseismic slip is observed in different geothermal fields like in Brawley (Wei et al., 2015) or at Soultz-Sous-Forêts (Cornet et al., 1997; Schoenball et al., 2014). Recent studies demonstrated that the contribution of aseismic motion could even be larger than the deformation through induced seismicity (De Barros et al., 2019; Duboeuf et al., 2017; Guglielmi et al., 2015). Coming back to the apparent disagreement between some of the modelling results and the observations, we now speculate that there is either a high probability of aseismic motion in the regions, which may explain the modelling suggested slip, or that there is a higher chance of seismicity to occur in this region in the future. Additional, independent observations from e.g. GPS measurements are required to shed light into these speculations.

6.3. Modelling considerations

The discussion above shows that the simulation model can contribute to the understanding of coupled hydromechanical processes interacting with deformation along preexisting faults. At the same time, the current model has severe limitations. While a friction model incorporating stable and unstable slip could be introduced in the simulation
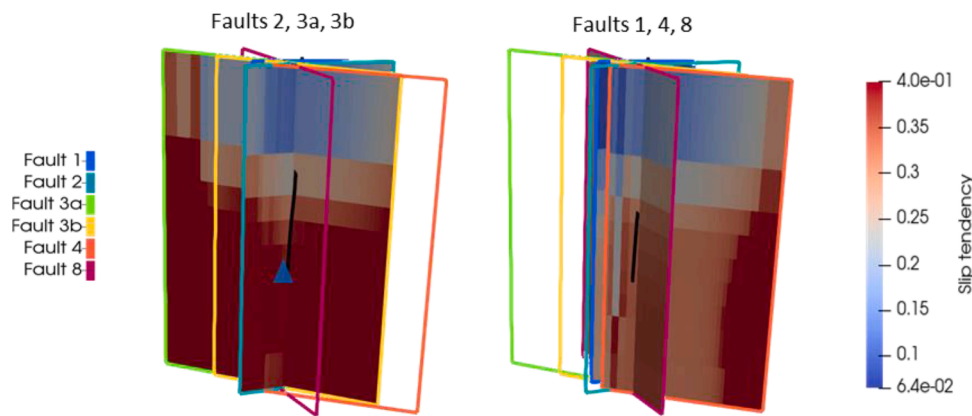
Table 2
Hydraulic rock parameters for the three different cases.

	Case A	Case B	Case C
Matrix permeability K_M [m²]	1e-12	2e-12	1e-11
Hydraulic aperture a [m]	1e-2	1e-2	1e-2
Tangential conductivity fault 1-4	$a^3/12$	$a^3/12$	$a^3/12$
Normal conductivity fault 1-4	$a/6$	$a/6$	$a/6$
Tangential conductivity fault 8	$a^3/12$	$a \cdot K_M$	$1e-2 \cdot K_M \cdot a$
Normal conductivity fault 8	$a/6$	$K_M/(a/2)$	$1e-2 \cdot K_M/(a/2)$

Fig. 7. Slip tendency for Faults 2, 3a and 3b and Faults 1, 4 and 8 at the start of stimulation, computed for Case A. The location of the injection point is indicated by a blue triangle. (For interpretation of the references to color in this figure legend, the reader is referred to the web version of this article.)
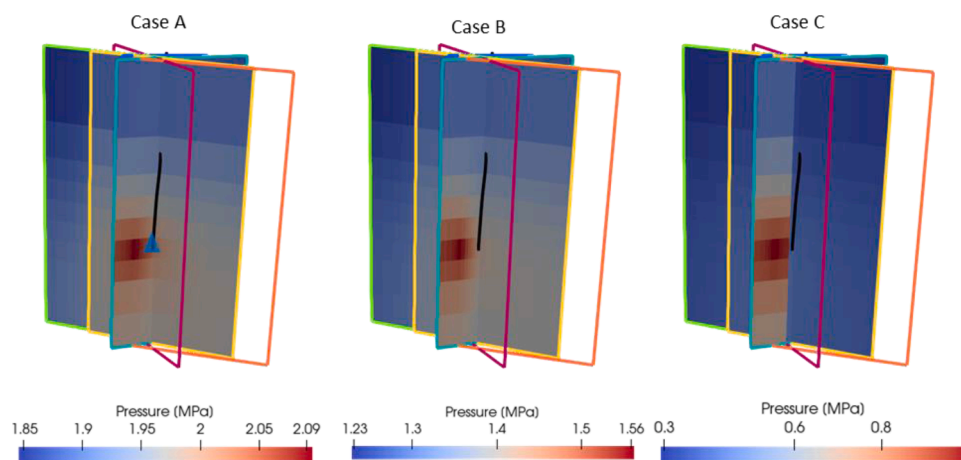

Fig. 8. Difference in pore pressure between the end of the cyclic stimulation and the initial state for Case A, Case B and Case C. Note that the scale of the pressure color bar is different for each of the three cases. The location of the injection point is indicated by a blue triangle. (For interpretation of the references to color in this figure legend, the reader is referred to the web version of this article.)

model to investigate this issue further, the available data is insufficient to parametrize such a refined model. While the local stress field before stimulation has strong influence on the extent to which faults are reactivated during the stimulation, the initialization process for the simulations is based on strong approximations, which are in turn based on fixed stress boundary conditions and a simple friction model. To limit model complexity in the light of available data, the simulation model also did not include aperture and permeability changes due to shear dilation, which can have a substantial impact on the flow properties of the faults (Berre et al., 2020). These aspects, along with the high uncertainty in model parameters, indicate significant model error.

Among these uncertainties, fault network geometry plays an important role as it can strongly affect connectivity. For example, the representation of faults as linear (in the horizontal plane) in the simulation model leads to a crossing of Faults 2 and 3a which is not manifest in fault traces mapped at the surface. Furthermore, a cross-cutting relationship between different fault sets at depth largely affects connectivity. However, modelling allows testing of different geometries, comparing the outcomes, and linking them with observations. As the seismic cloud during stimulation is located mainly to the north of Fault 8, on the same side of the fault as the fluid injection, a simple scenario-based study was designed to investigate the effect of varying the relative permeability of Fault 8 compared to the other faults and the matrix. For Case A, Fault 8 had a high permeability equal to that of the other faults; in Case B, it had a permeability equal to that of the matrix; and in Case C, it had a permeability significantly lower than the matrix. There is

significant difference in maximum accumulated slip along the active faults in the different cases, with longest slip in Case A and shortest in Case C. In Cases A and B, the regions of the faults that have slipped are similar and have similar slip profiles. The reason is likely that the faults are already critically stressed when injection starts, so that only small change in fluid pressure or poroelastic stress state will induce additional slip, which will redistribute poroelastic stress and further affect slip tendencies. For Case C, the effect of Fault 8 as a barrier to flow and the higher matrix permeability relative to Cases A and B can clearly be seen on Fault 2. The higher matrix permeability results in pressure migrating more easily into the matrix and lower pressures in all faults, including Fault 2 as compared in Cases A and B. At the same time, considering the large difference in results when changing the permeability of structures in the formation, slip distances along the active faults are clearly sensitive to the permeabilities of the faults and the matrix. Due to limitations in available data, the permeability of all faults (except Fault 8 in Cases B and C) was set as equal. Given that the NNE-striking to NE-striking structures (including Fault 1) display an aperture in the televiewer and that Fault 1 was deduced as open from the outcrop study (Khodayar et al., unpublished report, Supporting Material, Text S2), an alternative scenario could differentiate these fault sets from those that are ENE-striking (Faults 3a, 3b, and 4). This scenario is further supported by considering the normal load on the two sets of structures. Furthermore, the model is set up considering explicit representation of only six planar faults, while the actual fault geometry of the formation is richer, with larger-scale structures that are not resolved with the current
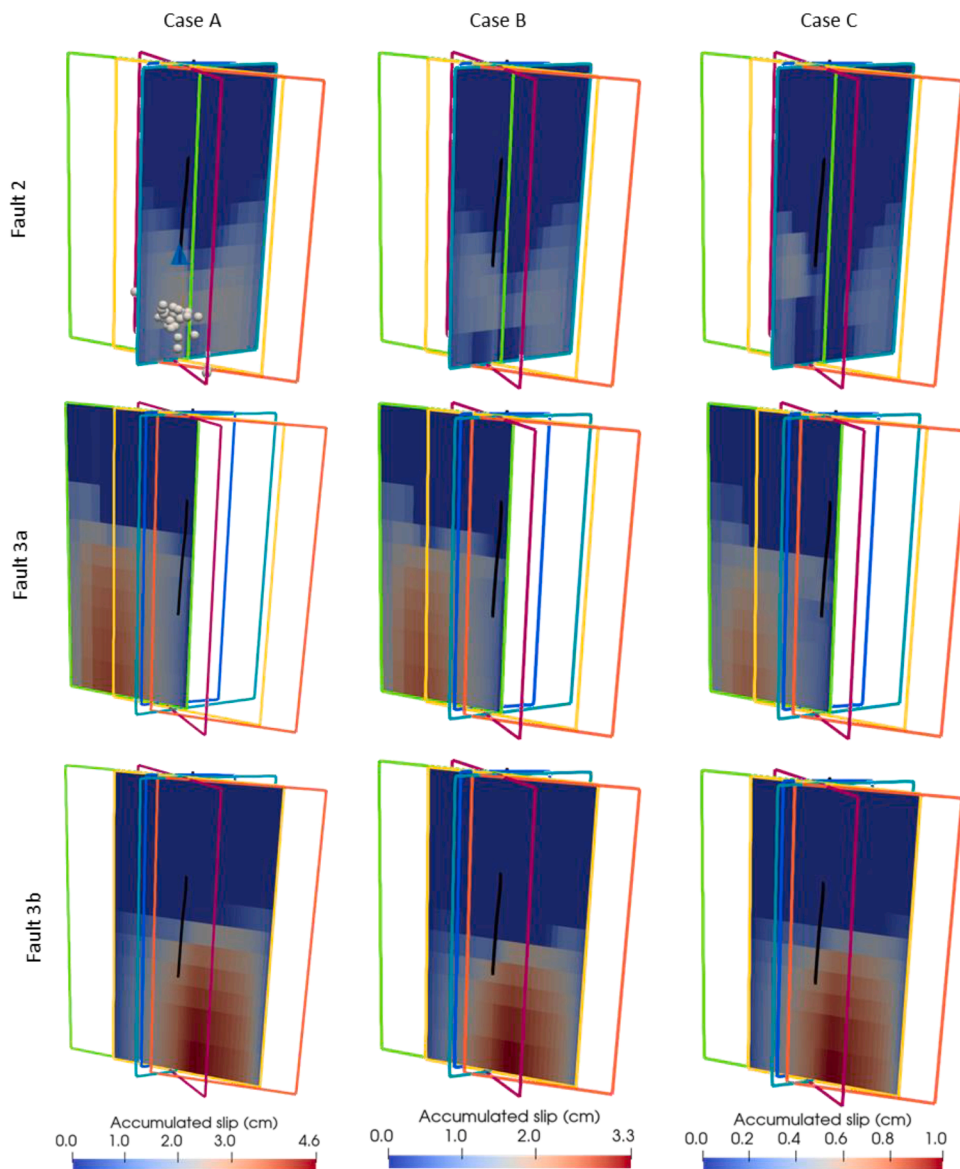
Fig. 9. Accumulated slips at the end of the stimulation with Cases A, B, and C in the first, second, and third column, respectively, and Faults 2, 3a, and 3b in the first, second and third row, respectively. The color bars (bottom) apply column-wise. Note that the scale of the color bar is different for each of the three cases. The upper left Fig. also shows the observed seismic events, as discussed in Section 3.2, and the location of the injection point (blue triangle). For the legend for fault numbers and orientation of north, see Fig. 6. (For interpretation of the references to color in this figure legend, the reader is referred to the web version of this article.)

model. Finally, the choice of a static friction and ignoring dilation of fractures with slip is also a simplification of the real situation.

7. Conclusion

Combining analysis of seismicity observed during well stimulation with simulation of injection-induced coupled hydro-mechanical processes, including explicit modeling of fault reactivation and slip, has the potential to improve our understanding of injection-induced fault reactivation. Considering a case study from Reykjanes, Iceland, we have presented a workflow where we first used new analysis of seismic data to establish a revised fault model before this model was used in simulation experiments. Reciprocally, the simulation results show how modelling can be used as a tool to improve interpretations from seismic analysis, e. g., in discriminating slip along close-by and similarly oriented faults. The test cases investigated also show how sensitive fault slip is to the initial stress state as well as the permeability of the faults and their surrounding formation. The results show how modelling and interpretation of seismic data jointly can give a better understanding of the hydro-mechanical processes taking place in stimulation of geothermal reservoirs. This provides an important step forward in understanding coupled hydro-mechanical processes and fault reactivation in hydraulic

stimulation of geothermal reservoirs, a task which requires interdisciplinary approaches and the combination of data analysis and physics-based simulation models.

Limitations of the current work are related to uncertainty in geological characterization and seismic analysis and model error. While the model framework allows for the introduction of more complex physics, this would lead to over-parameterization as the data are insufficient for identification of the additional parameters. For the seismic analysis, downhole monitoring instrumentation would allow for more precise event locations that could be used to inform the fault model. Furthermore, additional data from pressure transient testing with downhole pressure measurements would improve calibration of permeabilities for the different structural components of the model.

CRediT authorship contribution statement

Eirik Keilegavlen: Conceptualization, Methodology, Writing – original draft, Software, Formal analysis, Visualization, Supervision. **Laure Duboeuf:** Formal analysis, Methodology, Visualization, Writing – original draft. **Anna Maria Dichiarante:** Formal analysis, Methodology, Visualization, Writing – original draft. **Sæunn Halldórsdóttir:** Writing – review & editing. **Ivar Stefansson:** Software, Validation, Writing –

Declaration of Competing Interest

The authors declare that they have no known competing financial interests or personal relationships that could have appeared to influence the work reported in this paper.

Data availability

Source code and run scripts for the simulations in this paper are openly available under Version 3 of the GPL license (Keilegavlen & Stefansson, 2020).

The seismic data from the TS network used in this study is described by Jousset et al. (2020) and can be accessed through the frame of GEOFON, including metadata and seismic waveforms (https://geofon.gfz-potsdam.de/doi/network/4L/2014).

The seismic data from the PS network used in this study is owned by HS Orka and is confidential. Request for access to this data can be directed to HS Orka.

Additional information to aid reproducibility of results is provided in the Supporting Material.

Supplementary materials

Supplementary material associated with this article can be found, in the online version, at doi:10.1016/j.geothermics.2021.102223.

Appendix

This section provides the governing equations that underlies the simulation model used in the paper.

To fix the notation, we let subscripts M, F and I denote quantities in the rock matrix, fault network and fault intersections, respectively. Let the D-dimensional simulation domain Ω be decomposed into the rock matrix Ω_M, the fault network Ω_F of dimension $D-1$ and the intersections Ω_I of dimension $D-2$. The interface between Ω_M and Ω_F is denoted Γ, which can be split into its two sides Γ^+ and Γ^-.

Conservation of momentum and fluid mass in Ω_M are given by (Coussy, 2003)

$$\nabla \cdot (\mathscr{C}_M \nabla_s u_M - \alpha_M p_M I) = b_M,$$

$$\alpha_M \frac{\partial (\nabla \cdot u_M)}{\partial t} + \frac{1}{M} \frac{\partial p_M}{\partial t} - \nabla \cdot \left(\frac{\mathscr{K}_M}{\mu_M} \nabla p_M \right) = f_M.$$

Here, u_M and p_M are the deformation and fluid pressure in the rock matrix, $\mathscr{C}_M$ denotes the elastic moduli, ∇_s is the symmetric gradient, α_M Biot's coefficient. I is the identity matrix, $\frac{1}{M}$ represent the Biot modulus, $\mathscr{K}_M$ the rock permeability and μ is the (dynamic) fluid viscosity. Finally, b_M are body forces while f_M are source and sink terms for the fluid.

For momentum conservation in Ω_M, the displacement on the fracture-matrix interface, u_Γ, enters as Dirichlet boundary conditions. Fracture deformation is measured in terms of the jump in u_Γ, defined by $[[u_j]] = u_\Gamma^+ - u_\Gamma^-$, where $u_\Gamma^\pm$ is the deformation on $\Gamma^\pm$. The jump can be divided into its normal and tangential components, denoted $[[u_j]]_n$ and $[[u_j]]_\tau$, respectively. The mechanical state in Ω_F is described by the contact traction T_C, with tangential and normal components $T_{C,\tau}$ and $T_{C,n}$, respectively.

Fluid flow inside fault planes in Ω_F is governed by

$$\theta \frac{\partial p_F}{\partial t} - \nabla \cdot \left(\frac{\mathscr{K}_F}{\mu} \nabla p_F \right) - [[\lambda_{MF}]] = f_F.$$

Here, θ denotes fluid compressibility, while the flux between matrix and faults is represented by $\lambda_{MF} = \kappa(tr\, p_M - p_F)$, where κ is the normal permeability of the fracture, while $tr\, p_M$ gives the matrix pressure at the fracture wall, see Martin et al. (2005) for details. The jump $[[\lambda]]$ over the fault gives net flux from the matrix into the fault. Fluid flow in fault intersections is governed by a similar equation, with a term λ_{FI} that represent flow between fault and intersections. For details, see e.g. Nordbotten et al. (2019).

Finally, the relation between the contact forces T_C, the stress on the fracture walls and the fluid pressure in fractures and matrix are modeled with techniques from contact mechanics: Balance between the poro-elastic forces in fractures and matrix are expressed as

$$(\mathscr{C} \nabla_s u_M - \alpha I p_M) \cdot n = (T_C - p_F n)$$

Where n is the normal vector of Γ. In the normal direction, the contact stress is zero only when the jump is non-zero, that is
$$[[u_\Gamma]]_n \leq 0, \quad T_{C,n} \leq 0, \quad [[u_\Gamma]]_n T_{C,n} = 0.$$
In the tangential direction, the motion is determined by the relation between the tangential forces $T_{C,\tau}$ and the available friction forces $FT_{C,n}$, where F is the friction coefficient; the jump is zero until the friction force is overcome, in which case the motion is parallel to the tangential force:

$$||T_{C,\tau}|| \leq -FT_{C,n},$$

$$||T_{C,\tau}|| < -FT_{C,n} \rightarrow \left[\left[\dot{u}_\Gamma \right]\right]_\tau = 0,$$

$$||T_{C,\tau}|| = -FT_{C,n} \rightarrow \exists \alpha \in \mathbb{R}, \; T_{C,\tau} = -\alpha^2 \left[\left[\dot{u}_\Gamma \right]\right]_\tau,$$

see (Berge et al., 2020; Keilegavlen et al., 2021) for details. Based on the friction law above, the fault's slip tendency is given as $\| T_{C,\tau} \| / (- F T_{C,n})$, with maximum value equal to the friction coefficient occurring for a slipping fault.

References

Aavatsmark, I., 2002. An introduction to multipoint flux approximations for quadrilateral grids. Comput. Geosci. 6 (3–4), 405–432. https://doi.org/10.1023/A:1021291114475.

Baisch, S., Vörös, R., Rothert, E., Stang, H., Jung, R., Schellschmidt, R., 2010. A numerical model for fluid injection induced seismicity at Soultz-sous-Forêts. Int. J. Rock Mech. Min. Sci. 47 (3), 405–413. https://doi.org/10.1016/j.ijrmms.2009.10.001.

Batir, J., Davatzes, N.C., Asmundsson, R., 2012. Preliminary model of fracture and stress state in the Hellisheidi Geothermal Field, Hengill Volcanic System, Iceland. In: Proceedings of the 37th Workshop on Geothermal Engineering. Stanford.

Berge, R.L., Berre, I., Keilegavlen, E., Nordbotten, J.M., Wohlmuth, B., 2020. Finite volume discretization for poroelastic media with fractures modeled by contact mechanics. Int. J. Numer. Methods Eng. 121 (4), 644–663. https://doi.org/10.1002/nme.6238.

Berre, I., Doster, F., Keilegavlen, E., 2019. Flow in fractured porous media: A review of conceptual models and discretization approaches. Transp. Porous Media 130 (1), 215–236. https://doi.org/10.1007/s11242-018-1171-6.

Berre, I., Stefansson, I., Keilegavlen, E., 2020. Fault slip in hydraulic stimulation of geothermal reservoirs: Governing mechanisms and process-structure interaction. The Leading Edge 39 (12), 893–900. https://doi.org/10.1190/tle39120893.1.

Bjarnason, I.T., Menke, W., Flóvenz, Ó.G., Caress, D., 1993. Tomographic image of the mid-Atlantic plate boundary in southwestern Iceland. J. Geophys. Res.: Solid Earth 98 (B4), 6607–6622. https://doi.org/10.1029/92JB02412.

Björnsson, S., Einarsson, G.P., Tulinius, H., Hjartardóttir, Á.R., 2020. Seismicity of the Reykjanes Peninsula 1971–1976. J. Volcanol. Geotherm. Res. 391, 106369 https://doi.org/10.1016/j.jvolgeores.2018.04.026.

Blanck, H., Jousset, P., Hersir, G.P., Ágústsson, K., Flóvenz, Ó.G., 2020. Analysis of 2014–2015 on- and off-shore passive seismic data on the Reykjanes Peninsula, SW Iceland. J. Volcanol. Geotherm. Res. 391, 106548 https://doi.org/10.1016/j.jvolgeores.2019.02.001.

Bodvarsson, R., Rognvaldsson, S.T., Jakobsdottir, S.S., Slunga, R., Stefansson, R., 1996. The SIL data acquisition and monitoring system. Seismol. Res. Lett. 67 (5), 35–46. https://doi.org/10.1785/gssrl.67.5.35.

Bruel, D., 2007. Using the migration of induced seismicity as a constraint for fractured hot dry rock reservoir modelling. Int. J. Rock Mech. Min. Sci. 44 (8), 1106–1117. https://doi.org/10.1016/j.ijrmms.2007.07.001.

Brune, J.N., 1970. Tectonic stress and the spectra of seismic shear waves from earthquakes. J. Geophys. Res. 75 (26), 4997–5009. https://doi.org/10.1029/JB075i026p04997.

Byerlee, J., 1978. Friction of rocks. Pure Appl. Geophys. 116, 615–626. https://doi.org/10.1007/BF00876528.

Cappa, F., Scuderi, M.M., Collettini, C., Guglielmi, Y., Avouac, J.-P., 2019. Stabilization of fault slip by fluid injection in the laboratory and in situ. Sci. Adv. 5 (3), eaau4065 https://doi.org/10.1126/sciadv.aau4065 eaau4065.

Chabora, E., Zemach, E., Spielman, P., Drakos, P., Hickman, S., Lutz, S., 2012. Hydraulic stimulation of Well 27-15, Desert Peak Geothermal Field, Nevada, USA. In: Proceedings of the 37th Workshop on Geothermal Engineering. Stanford.

Clifton, A.E., Kattenhorn, S.A., 2006. Structural architecture of a highly obliquedivergent plate boundary segment. Tectonophysics 419 (1–4), 27–40. https://doi.org/10.1016/j.tecto.2006.03.016.

Cornet, F.H., Bérard, T., Bourouis, S., 2007. How close to failure is a granite rock mass at a 5 km depth? Int. J. Rock Mech. Min. Sci. 44 (1), 47–66.

Cornet, F.H., Helm, J., Poitrenaud, H., Etchecopar, A., 1997. Seismic and aseismic slips induced by large-scale fluid injections. In: Talebi, S. (Ed.), Seismicity Associated with Mines, Reservoirs and Fluid Injections. Birkhäuser Basel, Basel, pp. 563–583. https://doi.org/10.1007/978-3-0348-8814-1_12.

Coussy, Olivier, 2003. Poromechanics. John Wiley & Sons, Ltd.

De Barros, L., Cappa, F., Guglielmi, Y., Duboeuf, L., Grasso, J.-R., 2019. Energy of injection-induced seismicity predicted from in-situ experiments. Sci. Rep. 9 (1), 4999. https://doi.org/10.1038/s41598-019-41306-x.

Deichmann, N., Giardini, D., 2009. Earthquakes induced by the stimulation of an enhanced geothermal system below Basel (Switzerland). Seismol. Res. Lett. 80 (5), 784–798. https://doi.org/10.1785/gssrl.80.5.784.

Di Toro, G., Han, R., Hirose, T., De Paola, N., Nielsen, S., Mizoguchi, K., et al., 2011. Fault lubrication during earthquakes. Nature 471 (7339), 494–498. https://doi.org/10.1038/nature09838.

Duboeuf, L., De Barros, L., Cappa, F., Guglielmi, Y., Deschamps, A., Seguy, S., 2017. Aseismic motions drive a sparse seismicity during fluid injections into a fractured zone in a carbonate reservoir: injection-induced (a)seismic motions. J. Geophys. Res.: Solid Earth 122 (10), 8285–8304. https://doi.org/10.1002/2017JB014535.

Duboeuf, L., Oye, V., Dando, B.D., 2021. An Aggregated Template (AT) methodology: novel automatic phase-onset identification by template matching. Geophysical Prospecting. https://doi.org/10.1111/1365-2478.13103.

Ellsworth, W.L., 2013. Injection-induced earthquakes. Science 341 (6142), 1225942. https://doi.org/10.1126/science.1225942.

Ellsworth, W.L., Giardini, D., Townend, J., Ge, S., Shimamoto, T., 2019. Triggering of the Pohang, Korea, earthquake (Mw 5.5) by enhanced geothermal system stimulation. Seismol. Res. Lett. 90 (5), 1844–1858. https://doi.org/10.1785/0220190102.

Flovenz, O., Augustsson, K., Guðnason, E.Á., Kristjansdottir, S., 2015. Reinjection and induced seismicity in geothermal fields in Iceland. In: Proceedings of the World Geothermal Congress.

Gallyamov, E., Garipov, T., Voskov, D., van den Hoek, P., 2018. Discrete fracture model for simulating waterflooding processes under fracturing conditions. Int. J. Numer. Anal. Methods Geomech. 42 (13), 1445–1470. https://doi.org/10.1002/nag.2797.

Garipov, T.T., Hui, M.H., 2019. Discrete fracture modeling approach for simulating coupled thermo-hydro-mechanical effects in fractured reservoirs. Int. J. Rock Mech. Min. Sci. 122, 104075 https://doi.org/10.1016/j.ijrmms.2019.104075.

Garipov, T.T., Karimi-Fard, M., Tchelepi, H.A., 2016. Discrete fracture model for coupled flow and geomechanics. Comput. Geosci. 20 (1), 149–160. https://doi.org/10.1007/s10596-015-9554-z.

Genter, A., Evans, K., Cuenot, N., Fritsch, D., Sanjuan, B., 2010. Contribution of the exploration of deep crystalline fractured reservoir of Soultz to the knowledge of Enhanced Geothermal Systems (EGS). C.R. Geosci. 342 (7–8), 502–516. https://doi.org/10.1016/j.crte.2010.01.006.

Ghassemi, A., Tarasovs, S., Cheng, A.D., 2005. Integral equation solution of heat extraction-induced thermal stress in enhanced geothermal reservoirs. Int. J. Numer. Anal. Methods Geomech. 29 (8), 829–844. https://doi.org/10.1002/nag.440.

Grant, M.A., Clearwater, J., Quinão, J., Bixley, P.F., Le Brun, M., 2013. Thermal stimulation of geothermal wells: a review of field data. In: Proceedings of the Stanford Geothermal Workshop.

Grigoli, F, Cesca, S., Rinaldi, A.P., Manconi, A., López-Comino, J.A., Clinton, J.F., et al., 2018. The November 2017 Mw 5.5 Pohang Earthquake: a possible case of induced seismicity in South Korea. Science 360 (6392), 1003–1006. https://doi.org/10.1126/science.aat2010.

Guðnason, E.Á., 2014. Analysis of seismic activity on the western part of the Reykjanes Peninsula, SW Iceland. Master's thesis). University of Iceland. December 2008–May 2009.

Guglielmi, Y., Cappa, F., Avouac, J.-P., Henry, P., Elsworth, D., 2015. Seismicity triggered by fluid injection-induced aseismic slip. Science 348 (6240), 1224–1226. https://doi.org/10.1126/science.aab0476.

Häring, M.O., Schanz, U., Ladner, F., Dyer, B.C, 2008. Characterisation of the Basel 1 enhanced geothermal system. Geothermics 37 (5), 469–495. https://doi.org/10.1016/j.geothermics.2008.06.002.

Hakimhashemi, A.H., Schoenball, M., Heidbach, O., Zang, A., Grünthal, G., 2014. Forward modelling of seismicity rate changes in georeservoirs with a hybrid geomechanical–statistical prototype model. Geothermics 52, 185–194. https://doi.org/10.1016/j.geothermics.2014.01.001.

Hüeber, S., Stadler, G., Wohlmuth, B., 2008. A primal-dual active set algorithm for three-dimensional contact problems with Coulomb Friction. SIAM J. Sci. Comput. 30 (2), 572–596. https://doi.org/10.1137/060671061.

Izadi, G., Elsworth, D., 2014. Reservoir stimulation and induced seismicity: Roles of fluid pressure and thermal transients on reactivated fractured networks. Geothermics 51, 368–379. https://doi.org/10.1016/j.geothermics.2014.01.014.

Janecke, S.U., Evans, J.P., 1988. Feldspar-influenced rock rheologies. Geology 16 (12), 1064–1067. https://doi.org/10.1130/0091-7613(1988)016. <1064:FIRR>2.3.CO;2.

Jousset, P., Blanck, H., Franke, S., Metz, M., Augustsson, K., Verdel, A., et al., 2016. Seismic tomography in Reykjanes, SW Iceland. In: Proceedings of the European Geothermal Congress.

Jousset, P., Hersir, G.P., Blanck, H., Kirk, H., Erbas, K., Hensch, M., Franke, S., Bruhn, D., Huenges, E., 2020. IMAGE (Integrated Methods for Advanced Geothermal Exploration). Deutsches GeoForschungsZentrum GFZ. https://doi.org/10.14470/9Y7569325908.

Julian, B.R., Miller, A.D., Foulger, G.R., 1998. Non-double-couple earthquakes 1. Theory. Rev. Geophys. 36 (4), 525–549. https://doi.org/10.1029/98RG00716.

Juncu, D., Árnadóttir, T., Geirsson, H., Guðmundsson, G.B., Lund, B., Gunnarsson, G., et al., 2020. Injection-induced surface deformation and seismicity at the Hellisheidi geothermal field, Iceland. J. Volcanol. Geotherm. Res. 391 (1), 106337 https://doi.org/10.1016/j.jvolgeores.2018.03.019.

Kanji, M.A., 1974. The relationship between drained friction angles and Atterberg limits of natural soils. Géotechnique 24 (4), 671–674. https://doi.org/10.1680/geot.1974.24.4.671.

Keiding, M., Lund, B., Árnadóttir, T., 2009. Earthquakes, stress, and strain along an obliquely divergent plate boundary: Reykjanes Peninsula, Southwest Iceland. J. Geophys. Res.: Solid Earth 114 (B9), B09306. https://doi.org/10.1029/2008JB006253.

Keilegavlen, E., Berge, R., Fumagalli, A., Starnoni, M., Stefansson, I., Varela, J., Berre, I., 2021. PorePy: An open-source software for simulation of multiphysics processes in fractured porous media. Comput. Geosci. 25, 243–265. https://doi.org/10.1007/s10596-020-10002-5.

Keilegavlen, E., Stefansson, I., 2020. Keileg/RN-34-Stimulation: Simulation of Hydraulic Stimulation (version v1.0). Zenodo. https://doi.org/10.5281/ZENODO.4005633.

Khodayar, M., Björnsson, S., Guðnason, E.Á., Níelsson, S., Axelsson, G., Hickson, C., 2018. Tectonic control of the Reykjanes geothermal field in the oblique rift of SW Iceland: from regional to reservoir scales. Open J. Geol. 08 (03), 333–382. https://doi.org/10.4236/ojg.2018.83021.

Kim, K.-H., Ree, J.-H., Kim, Y.H., Kim, S., Kang, S.Y., Seo, W., 2018. Assessing whether the 2017 Mw 5.4 Pohang Earthquake in South Korea was an induced event. Science 360 (6392), 1007–1009. https://doi.org/10.1126/science.aat6081 eaat6081.

Klein, F.W., Einarsson, P., Wyss, M., 1977. The Reykjanes Peninsula, Iceland, earthquake swarm of September 1972 and its tectonic significance. J. Geophys. Res. 82 (5), 865–888. https://doi.org/10.1029/JB082i005p00865.

Kohl, T., Mégel, T., 2007. Predictive modeling of reservoir response to hydraulic stimulations at the European EGS site Soultz-Sous-Forêts. Int. J. Rock Mech. Min. Sci. 44 (8), 1118–1131. https://doi.org/10.1016/j.ijrmms.2007.07.022.

Kolditz, O., Clauser, C., 1998. Numerical simulation of flow and heat transfer in fractured crystalline rocks: application to the hot dry rock site in Rosemanowes (U.K.). Geothermics 27 (1), 1–23. https://doi.org/10.1016/S0375-6505(97)00021-7.

Kwiatek, G., Ben-Zion, Y., 2013. Assessment of P and S wave energy radiated from very small shear-tensile seismic events in a deep South African mine. J. Geophys. Res.: Solid Earth 118 (7), 3630–3641. https://doi.org/10.1002/jgrb.50274 no.

Langet, N., Goertz-Allmann, B., Oye, V., Bauer, R.A., Williams-Stroud, S., Dichiarante, A. M., Greenberg, S.E., 2020. Joint focal mechanism inversion using downhole and surface monitoring at the Decatur, Illinois, CO_2 injection site. Bull. Seismol. Soc. Am. 110 (5), 2168–2187.

Martin, Vincent, Jaffré, Jerome, Roberts E, Jean, 2005. Modeling Fractures and Barriers as Interfaces for Flow in Porous Media. SIAM J. Sci. Comput. 26, 1667–1691. https://doi.org/10.1137/S1064827503429363.

McClure, M.W., Horne, R.N., 2011. Investigation of injection-induced seismicity using a coupled fluid flow and rate/state friction model. Geophysics 76 (6), WC181–WC198. https://doi.org/10.1190/geo2011-0064.1.

Moeck, I., Kwiatek, G., Zimmermann, G., 2009. Slip tendency analysis, fault reactivation potential and induced seismicity in a deep geothermal reservoir. J. Struct. Geol. 31 (10), 1174–1181. https://doi.org/10.1016/j.jsg.2009.06.012.

Mukuhira, Y., Asanuma, H., Niitsuma, H., Häring, M.O., 2013. Characteristics of large-magnitude microseismic events recorded during and after stimulation of a geothermal reservoir at Basel, Switzerland. Geothermics 45, 1–17. https://doi.org/10.1016/j.geothermics.2012.07.005.

Nielsson, S., Eggertson, G., Weisenberger, T.B., Tulinius, H., Gudnason, E.Á., Friedleifson, G., 2020. The Reykjanes geothermal system—an extended conceptual model. In: Proceedings of the World Geothermal Congress.

Norbeck, J.H., McClure, M.W., Lo, J.W., Horne, R.N., 2016. An embedded fracture modeling framework for simulation of hydraulic fracturing and shear stimulation. Comput. Geosci. 20 (1), 1–18. https://doi.org/10.1007/s10596-015-9543-2.

Nordbotten, J.M., 2016. Stable cell-centered finite volume discretization for Biot Equations. SIAM J. Numer. Anal. 54 (2), 942–968. https://doi.org/10.1137/15M1014280.

Nordbotten, J.M., Boon, W.M., Fumagalli., A., Keilegavlen, E, 2019. Unified approach to discretization of flow in fractured porous media. Comput. Geosci. 23 (2), 225–237. https://doi.org/10.1007/s10596-018-9778-9.

Nordbotten, J.M., Keilegavlen, E., 2021. An introduction to multi-point flux (MPFA) and stress (MPSA) finite volume methods for thermo-poroelasticity. In: *Polyhedral Methods in Geosciences*. Springer, Cham, pp. 119–158.

Peter-Borie, M., Loschetter, A., Merciu, I.A., Kampfer, G., Sigurdsson, O., 2018. Borehole damaging under thermo-mechanical loading in the RN-15/IDDP-2 Deep Well: towards validation of numerical modeling using logging images. Geotherm. Energy 6, 17. https://doi.org/10.1186/s40517-018-0102-7.

Rahman, M.K., Hossain, M.M., Rahman, S.S., 2002. A shear-dilation-based model for evaluation of hydraulically stimulated naturally fractured reservoirs. Int. J. Numer. Anal. Methods Geomech. 26 (5), 469–497. https://doi.org/10.1002/nag.208.

Rutqvist, J., Dobson, P.F., Garcia, J., Hartline, C., Jeanne, P., Oldenburg, C.M., Vasco, D. W., Walters, M., 2015. The northwest geysers EGS demonstration project, California: pre-stimulation modeling and interpretation of the stimulation. Math. Geosci. 47 (1), 3–29. https://doi.org/10.1007/s11004-013-9493-y.

Sæmundsson, K., Sigurgeirsson, M.Á., Friðleifsson, G.Ó., 2020. Geology and structure of the Reykjanes volcanic system, Iceland. J. Volcanol. Geotherm. Res. 391, 106501 https://doi.org/10.1016/j.jvolgeores.2018.11.022.

Schindler, M., Baumgärtner, J., Gandy, T., Hauffe, P., Hettkamp, T., Menzel, H., et al., 2010. Successful hydraulic stimulation techniques for electric power production in the Upper Rhine Graben, Central Europe. In: Proceedings of the World Geothermal Congress.

Stefansson, I., Berre, I., & Keilegavlen, E. (2020). A fully coupled numerical model of thermo-hydro-mechanical processes and fracture contact mechanics in porous media. ArXiv:2008.06289. http://arxiv.org/abs/2008.06289.

Schoenball, M., Dorbath, L., Gaucher, E., Wellman, F., Kohl, T., 2014. Change of stress regime during geothermal reservoir stimulation. Geophysical Research Letters 41, 1163–1170. https://doi.org/10.1002/2013GL058514.

Storn, R., Price, K., 1997. Differential evolution—a simple and efficient heuristic for global optimization over continuous spaces. J. Glob. Optim. 11 (4), 341–359. https://doi.org/10.1023/A:1008202821328.

Sun, Z.-X., Zhang, X., Xu, Y., Yao, J., Wang, H.-X., Lv, S., et al., 2017. Numerical simulation of the heat extraction in EGS with thermal-hydraulic-mechanical coupling method based on discrete fractures model. Energy 120, 20–33. https://doi.org/10.1016/j.energy.2016.10.046.

Sæmundsson, K., 1978. Fissure swarms and central volcanoes of the neovolcanic zones of Iceland in Crustal evolution in northern Britain and adjacent regions. Geol. J. Liverpool 10, 415–432.

Ucar, E., Berre, I., Keilegavlen, E., 2017. Postinjection normal closure of fractures as a mechanism for induced seismicity: postinjection fracture closure. Geophys. Res. Lett. 44 (19), 9598–9606. https://doi.org/10.1002/2017GL074282.

Ucar, E., Berre, I., Keilegavlen, E., 2018a. Three-dimensional numerical modeling of shear stimulation of fractured reservoirs. J. Geophys. Res.: Solid Earth 123 (5), 3891–3908. https://doi.org/10.1029/2017JB015241.

Ucar, E., Keilegavlen, E., Berre, I., Nordbotten, J.M., 2018b. A finite-volume discretization for deformation of fractured media. Comput. Geosci. 22 (4), 993–1007. https://doi.org/10.1007/s10596-018-9734-8.

Vavryčuk, V., 2014. Iterative joint inversion for stress and fault orientations from focal mechanisms. Geophys. J. Int. 199 (1), 69–77. https://doi.org/10.1093/gji/ggu224.

Vavryčuk, V., 2015. Earthquake mechanisms and stress field. Encyclopedia of Earthquake Engineering. Springer-Verlag Berlin, Heidelberg. https://doi.org/10.1007/978-3-642-36197-5_295-1.

Waldhauser, F., 2000. A double-difference earthquake location algorithm: method and application to the Northern Hayward Fault, California. Bull. Seismol. Soc. Am. 90 (6), 1353–1368. https://doi.org/10.1785/0120000006.

Weemstra, C., Obermann, A., Verdel, A., Paap, B., Blanck, H., Guðnason, E.Á, et al., 2016. Time-lapse seismic imaging of the Reykjanes Geothermal Reservoir. In: Proceedings of the European Geothermal Congress. Strasbourg, France.

Wei, S., Avouac, J.-P., Hudnut, K.W., Donnellan, A., Parker, J.W., Graves, R.W., et al., 2015. The 2012 Brawley swarm triggered by injection-induced aseismic slip. Earth Planet. Sci. Lett. 422, 115–125. https://doi.org/10.1016/j.epsl.2015.03.054.

Weisenberger, T.B., Harðarson, B.S, Mesfin, K.G., Einarsson, G.M., Níelsson, S., Zierenberg, R.A., Friðleifsson, G.Ó., 2019. The Iceland Deep Drilling Project at Reykjanes - 4.5 km deep drilling into supercritical conditions. In: Proceedings of the 44th Workshop on Geothermal Reservoir Engineering. Stanford University, Stanford, California. February 11-13, 2019, SGP-TR-214.

Wuestefeld, A., Greve, S.M., Näsholm, S.P., Oye, V., 2018. Benchmarking earthquake location algorithms: a synthetic comparison. Geophysics 83 (4). https://doi.org/10.1190/geo2017-0317.1. KS35–47.

Wynants-Morel, N., Cappa, F., De Barros, L., Ampuero, J.-P., 2020. Stress perturbation from aseismic slip drives the seismic front during fluid injection in a permeable fault. J. Geophys. Res.: Solid Earth 125, e2019JB019179. https://doi.org/10.1029/2019JB019179.

Zhao, P., Kühn, D., Oye, V., Cesca, S., 2014. Evidence for tensile faulting deduced from full waveform moment tensor inversion during the stimulation of the Basel enhanced geothermal system. Geothermics 52, 74–83. https://doi.org/10.1016/j.geothermics.2014.01.003.

Ziegler, M., Rajabi, M., Heidbach, O., Hersir, G.P., Ágústsson, K., Árnadóttir, S., Zang, A., 2016. The stress pattern of Iceland. Tectonophysics 674, 101–113. https://doi.org/10.1016/j.tecto.2016.02.008.

Zimmermann, G., Reinicke, A., 2010. Hydraulic stimulation of a deep sandstone reservoir to develop an enhanced geothermal system: laboratory and field experiments. Geothermics 39 (1), 70–77. https://doi.org/10.1016/j.geothermics.2009.12.003.